RSC Advances

PAPER

View Article Online
View Journal | View Issue

Cite this: *RSC Adv.*, 2026, **16**, 21530

Green synthesis of a manganese (oxyhydr) oxide nanocomposite, utilizing *Eriobotrya japonica* leaf extract for adsorbing methyl blue dye from water

Honar Salah Ahmed * and Raghad Yousif Mohammed

Manganese (oxyhydr) oxides (γ-Mn_3O_4 and α-MnOOH) were successfully synthesized using *Eriobotrya japonica* leaf extract *via* a green-synthesis technique. The synthesized nanomaterials exhibited a characteristic absorption peak at 302 nm with an optical bandgap of 3.71 eV. XRD analysis confirmed the formation of γ-Mn_3O_4 and α-MnOOH with an average crystallite size of 30.83 nm, while SEM images revealed a mixed morphology of nanoparticles and nanorods with an average particle size of 37.72 nm. EDS and elemental mapping verified the predominant presence of Mn and O. BET analysis showed a specific surface area of 2.58 m^2 g^{-1} with mesoporous characteristics. The green-synthesized manganese (oxyhydr) oxide nanocomposite demonstrated high adsorption efficiency toward methyl blue dye, achieving a maximum removal of 91.95% at an initial dye concentration of 133.33 mg L^{-1}. Adsorption equilibrium followed the Langmuir isotherm (R^2 = 0.9846, q_{max} = 1138.2 mg g^{-1}), while kinetic data were best described by the pseudo-second-order model (R^2 > 0.99), confirming a chemisorption mechanism. Thermodynamic analysis indicated that the adsorption process is exothermic, spontaneous, and favorable. In addition, the adsorbent exhibited moderate reusability performance over multiple cycles, highlighting its stability and potential for sustainable wastewater treatment applications.

Received 21st January 2026
Accepted 28th March 2026

DOI: 10.1039/d6ra00547k

rsc.li/rsc-advances

Introduction

Global environmental concerns have intensified in recent years due to rapid population growth, urbanization, and industrial development, which have significantly altered consumption patterns and resource utilization. These changes have resulted in the large-scale generation of municipal and industrial wastes, posing serious environmental challenges. Among them, wastewater contamination by dyes and heavy metals represents a major threat to ecosystems and human health. Improper disposal and insufficient treatment of industrial and domestic effluents introduce a wide range of organic pollutants into water, soil, and the atmosphere. Therefore, the development of effective wastewater treatment strategies has become an urgent and widely researched priority. Due to their chemically stable structures, dyes persist in aquatic systems, reducing dissolved oxygen levels and disrupting aquatic life. They also can produce toxic, carcinogenic, and mutagenic byproducts, posing serious risks to both environmental and human health.[1,2] Methyl blue dye (MB), with the molecular formula $C_{37}H_{28}N_3Na_2O_9S_3^+$, is a triphenylmethane and an anionic dye usually used in coloring, textiles, paper, inks, printing, cosmetics, fibers, and plastics.[3,4]

To address this challenge, several treatment methods such as coagulation, photocatalysis, membrane filtration, chemical and biological oxidation, and adsorption have been developed. Among these, adsorption is particularly attractive due to its high efficiency, low cost, simple operation, reduced energy requirements, and minimal secondary waste generation.[5] Many different adsorbents were utilized to adsorb the pollutants and dyes from the wastewater, such as active carbon, zeolites, metal and metal oxide nanostructures, fly ash, clay, and functional polymeric materials.[6,7] The porous shape and functional groups of the adsorbents mainly affect the adsorption performance of organic dyes.[8]

Metal oxide (*e.g.*, ZnO, TiO_2, CuO, Ag_2O, Mn oxides, *etc.*) nanoparticles are the most studied material groups. They played a significant role in various fields of applications, among them as drug delivery systems, water purification, and anti-inflammatory and antibacterial activity.[9,10]

The basic unit of the crystal structure of manganese oxides is a MnO_6, comprising a central manganese atom surrounded by six oxygen atoms. The MnO_6 octahedra connect *via* edge-sharing to form single chains, leading to manganese oxides with diverse structures with edge-as well as corner-sharing.[11] Manganese oxides are typically classified into two different categories according to the arrangement of MnO_6: the layered structure, known as phyllomanganate, and the tunnelled structure, referred to as tectomanganate.[12,13] The layered

Department of Physics, College of Science, University of Duhok, Duhok 42001, Kurdistan Region, Iraq. E-mail: honar.ahmed@uod.ac; raghad.mohammed@uod.ac

structure comprises layers of edge-sharing MnO_6 octahedra, with symmetry dependent on the arrangement of Mn(III) octahedra. The tunnelled structure is formed by edge-sharing MnO_6 octahedra forming the walls, floor, and ceiling of the tunnels.[13] Heterovalent manganese ions, as well as foreign transition-metal cations, can be present inside both structures of manganese oxides, either replacing Mn(IV) or acting as charge compensators in phyllomanganate interlayers or tectomanganate tunnels.[14,15]

Typical instances of tunnelled structures of manganese oxides are todorokite, pyrolusite (β-MnO_2), groutite (α-MnOOH), feitknechtite (β-MnOOH), manganite (γ-MnOOH), and cryptomelane. In contrast, the layered manganese oxides have structures that include birnessite, buserite, and vernadite. The distinct manganese oxides exhibit a variety of sizes and crystal structures, leading to variations in redox reactions, adsorption, electrochemical, and photochemical processes.

Marokite (γ-Mn_3O_4) with an orthorhombic crystal structure, *Pbcm* symmetry (space group #57; $Z = 4$), and groutite (α-MnOOH) orthorhombic crystal structure and space group (*Pnma*; $Z = 4$) are manganese (oxyhydr) oxides that have received significant attention in the adsorption, oxidation, electrode of the batteries, and super capacitors.[16–21]

A variety of methods have been employed to synthesise different Mn oxide nanostructures, such as chemical, physical processes, and biological methods. Chemical methods, such as the sol–gel method,[22,23] hydrothermal/solvothermal method,[24] chemical vapour deposition (CVD),[25] physical methods such as laser ablation,[26] sputtering,[27] aerosols[28] and biological methods such as bacteria,[29] fungus,[30] yeast,[31] Actinomycetes,[32] algae,[33] plants (leaves, roots, fruit, peel).[34–36]

Phytonanotechnology is an emerging approach in agricultural biotechnology that enables the green synthesis of nanoparticles using plant-derived materials such as leaves, seeds, and peels. Plant extracts contain phytochemicals and metabolites that act as reducing and stabilizing agents during nanoparticle formation. Compounds such as flavonoids, organic acids, and quinones facilitate metal ion reduction, while polyphenols and tannins contribute to nanoparticle stabilization. Owing to its environmental friendliness, low cost, simplicity, scalability, and biocompatibility, this plant-based synthesis method has gained significant attention for producing metal and metal oxide nanomaterials.[37,38]

Loquat (*Eriobotrya japonica*) is a subtropical evergreen fruit tree that originated in southeastern China. It has been cultivated in China for more than 2000 years. The plant possesses significant medicinal value, and various parts of the tree have long been utilized in traditional medicine. In Chinese folk medicine, loquat extracts have been used to treat cough, chronic bronchitis (CB), inflammation, diabetes, and cancer, as documented in ancient texts such as the *Compendium of Materia Medica*.[39]

Eriobotrya japonica is rich in diverse phytochemicals, including phenols, alkaloids, cardiac glycosides, flavonoids, mucilage, gums, and phytosterols. The leaves and fruits contain numerous bioactive compounds such as vitamins, phenolic compounds, flavonoids, and carotenoids. In particular, loquat leaves contain phenolic acids, flavonoids, tannins, sesquiterpenes, triterpenes, and megastigmane glycosides. Bioactive triterpenoids such as oleanolic acid and ursolic acid are present in both flowers and leaves, although their concentrations vary depending on cultivar type and developmental stage.[40]

The chemical composition of loquat leaves is complex and diverse. Khouya *et al.* have been reported that loquat leaves contain substantial amounts of fiber, minerals (Ca, K, Na, and Fe), and vitamins, including B_2, B_6, and B_{12}.[41] According to Hwang *et al.*, the proximate composition of loquat leaves includes 8.78% moisture, 6.74% crude protein, 7.87% crude fat, 6.99% crude ash, 43.61% dietary fiber, and 26.01% carbohydrates. Their study also identified 16 amino acids and several fatty acids, such as lauric, myristic, pentadecanoic, stearic, and oleic acids.[42] Furthermore, Infante-Rodríguez, D. A. *et al.* reported that loquat leaves contain 0.039 mg vitamin A, 0.096 mg vitamin E, and 0.575 mg vitamin C, while the mineral composition follows the order Ca > K > Mg > Na > Fe > Mn > Zn.[43]

Phenolic compounds represent one of the most extensively investigated classes of phytochemicals in *E. japonica* leaves, with phenolic acids and flavonoids being the predominant groups. Additionally, more than 164 volatile compounds have been identified in the leaves (Taniguchi *et al.*, and Zhu *et al.*).[44,45] Various triterpenoids—including methyl betuliate, methyl maslinate, methyl corosolate, oleanolic acid, ursolic acid, maslinic acid, corosolic acid, tormentic acid, and euscaphic acid—have also been isolated from loquat leaves (Lv *et al.*, 2008).[46] Moreover, Chen *et al.*, identified several terpenoid compounds such as methoxy-euscophic acid, tormentic acid, methylcorosolate, corosolic acid, maslinic acid, oleanolic acid, and ursolic acid, along with phenolic–terpenoid derivatives including methoxy-3-*O*-*p*-coumaroyltormenic acid, 3-*O*-*p*-coumaroyltormenic acid, methoxy-3-*O*-*p*-coumaroylmaslinic acid, and 3-*O*-*p*-coumaroylmaslinic acid.[47]

The abundance of these phytochemicals, particularly phenolic compounds and flavonoids, makes loquat leaf extract a promising natural reducing and stabilizing agent for the green synthesis of nanomaterials.

In this work, marokite (γ-Mn_3O_4) and groutite (α-MnOOH) manganese (oxyhydr) oxides in nanoparticle and nanorod forms were synthesized *via* a green-synthesizing method using *Eriobotrya japonica* leaf extract and applied for methyl blue (MB) dye removal from water. The adsorption behavior was evaluated using Langmuir, Freundlich, Temkin, and Dubinin–Radushkevich isotherm models, while pseudo-first-order, pseudo-second-order, and intraparticle diffusion models were used to examine the adsorption kinetics. The obtained performance was compared with previously reported adsorbents, and the reusability of the green-synthesized nanocomposite was also assessed.

Materials and method

Manganese nitrate tetrahydrate $Mn(NO_3)_2 \cdot 4H_2O$, sodium hydroxide (NaOH) with a purity of greater than 99%, and methyl blue dye MB ($C_{37}H_{28}N_3Na_2O_9S_3^+$) with maximum absorption peak (λ_{max} = 600 nm) were acquired from Merck (Germany—

Darmstadt) and used for experiments without additional purification.

Collecting *Eriobotrya japonica* leaves

Collecting and extracting preparation of *Eriobotrya japonica* leaves. *Eriobotrya japonica* leaves (loquat), locally known as Askidinia, were collected in May 2024 from Duhok Governorate, Iraq (36.8632° N, 42.9885° E). The freshly harvested leaves were thoroughly washed several times with distilled water and then shade-dried at ambient conditions. After drying, the leaves were ground into a fine powder. The powdered material was extracted by mixing 1 g of leaf powder with 10 mL of distilled water and heating the mixture at 60 °C for 40 min. The resulting extract was filtered using Whatman no. 1 filter paper, and the filtrate was stored at 4 °C for subsequent use. A schematic representation of the EJLE preparation procedure is presented in Fig. 1.

Green-synthesis of manganese (oxyhydr) oxide nanocomposite

An aqueous solution of $Mn(NO_3)_2 \cdot 4H_2O$ (0.5 M) was prepared by dissolving 6.275 g of the salt in 50 mL of distilled water under continuous stirring for 5 min until complete dissolution was achieved. Subsequently, 25 mL of *Eriobotrya japonica* leaf extract (EJLE) was added gradually to the manganese nitrate solution in a dropwise manner. The pH of the resulting mixture was then adjusted using an appropriate volume of 0.1 M NaOH, followed by continuous stirring at room temperature for 30 min. The mixture was subsequently heated at 80 °C for 90 min with constant stirring. A noticeable change in the solution color from brown to dark indicated the formation of manganese (oxyhydr) oxide nanocomposite. The obtained product was then calcined at 400 °C for 2 h. Finally, the black powder was collected and stored for further characterization. The stepwise synthesis procedure of the manganese (oxyhydr) oxide nanocomposite is schematically presented in Fig. 2.

The synthesis of the green-synthesis of manganese (oxyhydr) oxide nanocomposite using *Eriobotrya japonica* leaf extract as an environmentally friendly reducing and capping agent proceeds through three main stages, as illustrated in Fig. 3. In the first stage, manganese ions (Mn^{2+}) derived from manganese nitrate tetrahydrate interact with bioactive molecules in the plant extract, particularly hydroxyl (–OH) and phenolic groups. These phytochemicals function as reducing agents by donating electrons, thereby reducing Mn^{2+} ions to elemental manganese (Mn^0) through a redox process.

In the second stage, the generated Mn^0 atoms undergo nucleation, resulting in the formation of small clusters. These clusters subsequently aggregate as a result of energy minimization, initiating nanoparticle growth. During the growth stage,

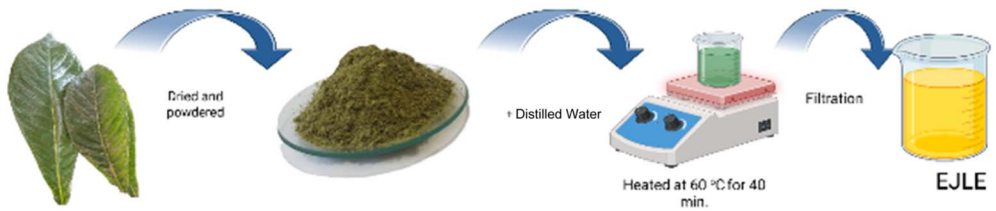

Fig. 1 The preparation steps of *Eriobotrya japonica* leaf extract (EJLE).

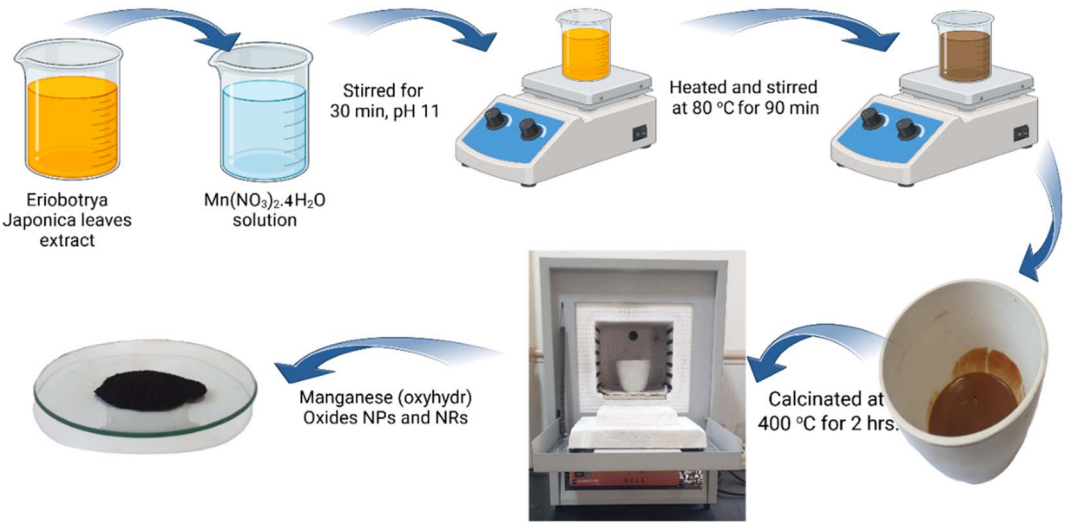

Fig. 2 Proposed step-by-step reaction mechanism for the green synthesis of Mn_3O_4/MnOOH composite nanomaterials using *Eriobotrya japonica* leaf extract as reducing, capping, and stabilizing agent.

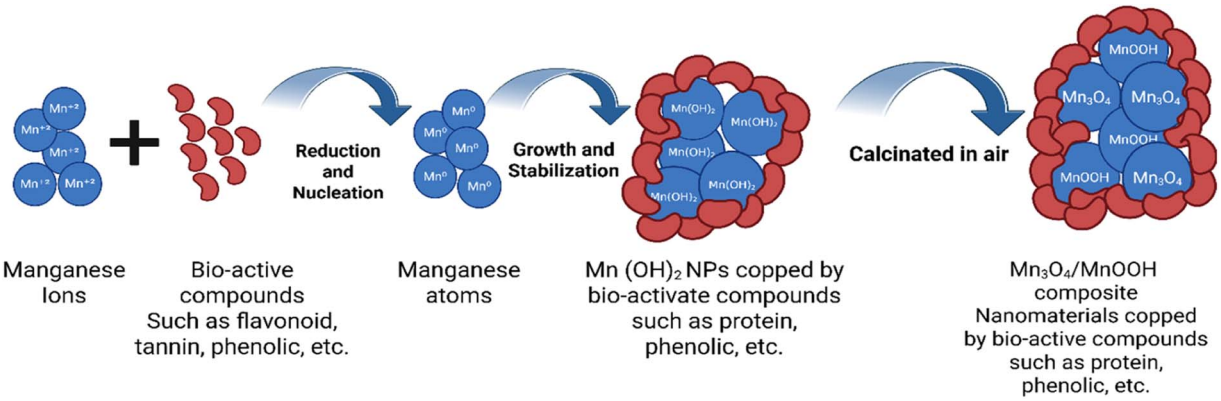

Fig. 3 The synthesis steps of manganese (oxyhydr) oxide nanocomposite using *Eriobotrya japonica* leaf extract.

smaller clusters merge into larger ones through the Ostwald ripening mechanism, which leads to the development of larger and more stable nanoparticles. The phytochemical constituents of the *Eriobotrya japonica* leaf extract, including polyphenols and flavonoids, play an important role in stabilizing the growing nanoparticles. In addition, carboxylic acid groups (–COOH) present in the extract may lose hydrogen atoms to form carboxylate ions ($–COO^-$), which attach to the nanoparticle surfaces. These carboxylate ions provide electrostatic and steric stabilization, preventing particle aggregation and helping to regulate the size and morphology of the nanoparticles.

In the final stage, the stabilized nanoparticles, which mainly consist of $Mn(OH)_2$ intermediates, undergo thermal decomposition during the calcination process. This thermal treatment converts the hydroxide intermediates into crystalline Mn_3O_4/MnOOH composite nanomaterials with a well-defined morphology.

Overall, this synthesis pathway highlights the important roles of polyphenols, flavonoids, and carboxylic acids present in *Eriobotrya japonica* leaf extract in the reduction, growth, and stabilization of the nanoparticles. These mechanisms are consistent with those proposed by Barzinjy *et al.*, for ZnO NPs,[48] Gebreslassie & Gebretnsae for SnO_2 NPs,[49] Miraeez S. A. and R. Y. Mohammed for CdO NPs.[50]

Phytochemical screening of *Eriobotrya japonica* leaf extract

Qualitative phytochemical screening of the *Eriobotrya japonica* leaf extract (EJLE) was carried out using standard chemical assays to identify the presence of major bioactive constituents.

Flavonoids test. Flavonoids were detected by adding a few drops of 10% lead acetate solution to the extract, where the formation of a yellow precipitate confirmed their presence.[51,52]

Carbohydrate test (CHO). Carbohydrates were examined using the Molisch test by mixing 1 mL of EJLE with five drops of α-naphthol solution, followed by the careful addition of 1 mL of concentrated H_2SO_4 along the test tube wall; the appearance of a violet ring indicated carbohydrates.[53]

Tannin test. Tannins were identified using Braymer's test, in which 1 mL of EJLE was diluted with 3 mL of distilled water and boiled, followed by the addition of 1 mL of 1% ferric chloride solution. A color change to blue-green, brownish-green, or bluish-black signified the presence of tannins.[54–56]

Alkaloids test (Hager's test). Alkaloids were assessed using Hager's test, where the formation of a creamy white precipitate after mixing the extract with a saturated picric acid solution indicated alkaloids.[57]

Saponin test (foam test). Saponins were detected using the foam test by vigorously shaking an appropriate amount of the extract with 3 mL of distilled water; persistent foam formation confirmed saponins.[58]

Phenolic test. Phenolic compounds were identified by adding 3 mL of 10% lead acetate solution to 5 mL of EJLE, where the appearance of a white precipitate indicated phenols.[59]

Protein and amino acid. Proteins and amino acids were examined using the ninhydrin test, in which the development of a purple coloration after adding 1 mL of 1% ninhydrin reagent to the extract confirmed the presence of amino acids.[60]

Adsorption activity test of green-synthesized manganese (oxyhydr) oxide nanocomposite

The adsorption performance of the green-synthesized manganese (oxyhydr) oxide nanocomposite for the removal of methyl blue (MB) dye from aqueous solutions was evaluated under dark conditions to exclude any photochemical effects. A series of MB solutions with initial concentrations of 133.33, 150, 166.67, 183.33, and 200 mg L^{-1} were prepared in 150 mL of distilled water, and their initial absorbance values were recorded using a JENWAY 6850 UV-vis spectrophotometer. Batch adsorption experiments were then carried out according to the experimental conditions summarized in Table 1. During the adsorption process, samples were collected at 3 min intervals. The withdrawn samples were centrifuged at 4000 rpm for 15 min to separate the nanocomposite, and the absorbance of the clear supernatant was subsequently measured using a UV-vis spectrophotometer to determine the residual MB concentration. The adsorption efficiency, adsorption capacity at time (t), and at equilibrium were calculated through the following equations:[61,62]

$$\text{adsorption effeciency} = \frac{(C_0 - C_t)}{C_0} \times 100\% \quad (1)$$

Table 1 Adsorption batch experiments for MB dye

Runs	pH	Initial concentration of MB dye (mg L^{-1})	Green-synthesized manganese (oxyhydr) oxides nanocomposite (mg/150 mL)	Temperature (K)
1	2	133.33	20	283
2	4	133.33	20	283
3	6	133.33	20	283
4	8	133.33	20	283
5	10	133.33	20	283
6	10	133.33	7.5	283
7	10	133.33	11.25	283
8	10	133.33	15	283
9	10	150	20	283
10	10	166.67	20	283
11	10	183.33	20	283
12	10	200	20	283
13	10	133.33	20	298
14	10	133.33	20	308

$$q_t = \frac{(C_0 - C_t)V}{W} \quad (2)$$

$$q_e = \frac{(C_0 - C_e)V}{W} \quad (3)$$

Here, C_0, C_t and C_e denote the initial, time-dependent, and equilibrium concentrations of methyl blue (MB) dye, respectively. V represents the volume of the MB solution (L), while W corresponds to the mass of the manganese (oxyhydr) oxide nanocomposite employed as the adsorbent. The parameters q_t and q_e refer to the adsorption capacity at a given time t and at equilibrium, respectively.

Adsorption isotherms

Adsorption isotherms are widely recognized as effective tools for elucidating the interaction between methyl blue (MB) dye as the adsorbate and manganese (oxyhydr) oxide nanocomposite as the adsorbent, as well as for describing the distribution of unadsorbed dye at equilibrium.[63] Different isotherm models provide insight into the distinct physical and chemical features governing the adsorption process. These models are valuable for optimizing adsorbent properties and for clarifying the underlying adsorption mechanism.[64] In this study, the Langmuir, Freundlich, Temkin, and Dubinin–Radushkevich (D–R) isotherms were applied to interpret the experimental data, enabling a comprehensive evaluation of MB dye adsorption onto manganese (oxyhydr) oxide nanocomposite. The suitability of each isotherm model was determined by comparing their respective correlation coefficient (R^2) values.

The Langmuir isotherm assumes that adsorption occurs through the formation of a homogeneous monolayer on the surface of the adsorbent, where all active sites are equivalent and possess the same adsorption energy. In this model, each site accommodates only one adsorbate molecule, and no interactions take place between the adsorbed species.[65] The linear Langmuir adsorption isotherm can be expressed as follows.[66,67]

$$\frac{C_e}{q_e} = \frac{1}{K_L q_{max}} + \frac{C_e}{q_{max}} \quad (4)$$

In this isotherm, q_{max} represents the maximum monolayer adsorption capacity, while C_e and q_e denote the equilibrium concentration and the corresponding adsorption capacity, respectively.

The Langmuir constant K_L (L mg^{-1}), which reflects the affinity and energy of the adsorption process, can be determined along with q_{max} from the linear plot of C_e *versus* C_e/q_e.

In addition, the dimensionless separation factor (R_L), a key parameter for evaluating the favorability of adsorption, is calculated using the following equation.[68]

$$R_L = \frac{1}{1 + C_0 \times K_L} \quad (5)$$

where R_L is the separation factor and K_L (L mg^{-1}) is the adsorption energy.

The dimensionless separation factor (R_L) is commonly used to evaluate the nature and feasibility of an adsorption process. Depending on its value, the adsorption behavior can be classified as unfavorable ($R_L > 1$), linear ($R_L = 1$), irreversible ($R_L = 0$), or favorable when R_L lies between 0 and 1.

The Freundlich isotherm assumes a heterogeneous adsorbent surface characterized by active sites with different energy levels, leading to the formation of multilayer adsorption rather than a uniform monolayer. The Freundlich isotherm could be stated as.[69]

$$\log q_e = \log k_f + \frac{1}{n} \log C_e \quad (6)$$

K_f, and $1/n$ are the Freundlich constants related to the adsorption process's capacity and intensity, respectively. The value of the $1/n$ can be equal to between 0 to 1, >1, and =0, which signifies the favorable, unfavorable, and irreversible of the adsorption process, respectively.[66] The values of n and K_f were calculated from the slope and intercept of the graph between $\log C_e$ and $\log q_e$.

The Temkin isotherm describes adsorption on a heterogeneous surface by accounting for adsorbate–adsorbent interactions while neglecting the effects at extremely low and high concentrations. It assumes that the heat of adsorption decreases linearly with increasing surface coverage as temperature rises, rather than following a logarithmic dependence.[70] The Temkin isotherm can be expressed as follows.[68]

$$q_e = B \ln A + B \ln C_e \quad (7)$$

were,

$$B = \frac{RT}{b_t} \quad (8)$$

where q_e, B, b_t, A, T, and R are the equilibrium adsorbed MB dye (mg g^{-1}), Temkin constant related to energy, Temkin constant of adsorption heat (J mol^{-1}), equilibrium binding constant (L mol^{-1}), temperature (K), and universal gas constant (8.314 J mol^{-1} K^{-1}), respectively. The values of Temkin constants, b_t and A_T, were calculated from the slope and intercept of the graph q_e *versus* $\ln C_e$.

Dubinin–Radushkevich (D–R) is typically employed to comprehend the mechanisms of adsorption, whether chemical or physical.[71] This semi-empirical adsorption isotherm is a temperature-dependent isotherm and is typically employed to represent the Gaussian energy distribution onto a heterogeneous adsorbent surface.[66] The value gives the vital information about the adsorption process, such as when the energy value is less than 8 kJ mol^{-1}, the process is physical adsorption, and when the energy value is between 8 and 16 kJ mol^{-1}, the process is the ion exchange, and is a chemical adsorption when the energy value is above 16 kJ mol^{-1}.[71] The equations of the D–R isotherm and energy can be written as follows.[68]

$$\ln q_e = \ln q_m - K_{DR}\varepsilon^2 \quad (9)$$

and,

$$\text{energy} = \frac{1}{\sqrt{2K_{DR}}} \quad (10)$$

where the polyani potential is, and can be calculated as.

$$\varepsilon = RT \ln\left(1 + \frac{1}{c_e}\right) \quad (11)$$

where K_{DR} (mol^2 kJ^{-2}) and q_m (mg g^{-1}) are the Dubinin–Radushkevich (D–R) constant and theoretical ability of adsorption, which could be calculated from the graph $\ln q_e$ *versus* ε^2. T and R are the temperature (K) and the universal gas constant (8.314 J mol^{-1} K^{-1}), respectively.

Adsorption kinetics

The adsorption kinetics were analyzed using the pseudo-first-order, pseudo-second-order, and intraparticle diffusion models, as these kinetic models provide valuable information about the adsorption equilibrium behavior.[72] In particular, the pseudo-first-order and pseudo-second-order models are widely used to elucidate the nature of interactions, whether physical or chemical, between adsorbate molecules and the adsorbent surface.[73] R^2 values have been used to evaluate the correlation between kinetic models and experimental results. The linear equations for the three models can be represented as follows.[67,74]

The pseudo-first-order kinetic model assumes that the rate of adsorption is directly proportional to the number of available active sites on the adsorbent surface and inversely related to the concentration of the adsorbate.[75] The pseudo-first-order kinetic can be written as shown below:

$$\ln(q_e - q_t) = \ln q_e - k_1 t \quad (12)$$

where q_e, q_t, k_1, and t are the equilibrium and initial concentrations of the MB dye (mg g^{-1}), rate constant (min^{-1}), and time (min), respectively. A plot of $\ln(q_e - q_t)$ *versus* time is used to calculate the values of q_e and k_1 from their intercept and slope, respectively.

The pseudo-second-order (eqn (13)) is utilized to investigate the chemisorption of the adsorbate and adsorbent.

$$\frac{t}{q_e} = \frac{1}{k_2 q_e^2} + \frac{t}{q_e} \quad (13)$$

where k_2 (g mg^{-1} min^{-1}) is the rate constant, and other parameters were defined above. The parameters q_e and k_2 can be calculated from the slope and intercept of the graph t/q_t *versus* t.

The intraparticle diffusion kinetic model was employed to understand the diffusion mechanism of the adsorption process.[70] The intraparticle diffusion model equation can be written as follows.[76]

$$q_t = k_{id} t^{0.5} + C \quad (14)$$

Here, k_{id} (g mg^{-1} $min^{-0.5}$) represents the intraparticle diffusion rate constant, while C corresponds to the boundary layer thickness. If intraparticle diffusion governs the adsorption process, a linear relationship passing through the origin should be observed. The parameters k_{id} and C can be determined from the slope and intercept, respectively, of the plot of q_t *versus* $t^{0.5}$.

Thermodynamic parameters

To evaluate the thermodynamic parameters and assess the effect of temperature on the adsorption of methyl blue onto manganese (oxyhydr) oxide nanocomposite, experiments were performed at different temperatures (283, 298, and 308 K), while maintaining constant conditions of dye concentration (133.33 mg L^{-1}), adsorbent dose (0.02 g), and pH (10). The thermodynamic quantities ΔH, ΔS, and ΔG were determined using the corresponding equations derived from the plot of $\ln K_{ads}$ *versus* $1/T$.

$$\ln K_{ads} = -\frac{\Delta H}{RT} + \frac{\Delta S}{R} \quad (15)$$

where K_{ads}, ΔH, ΔS, R, and T are the equilibrium constant of the adsorption, change in enthalpy, entropy change, universal gas

constant (8.314 J mol^{-1} K^{-1}), and temperature in (K), respectively.[77,78]

$$K_{ads} = \frac{q_e}{C_e} \quad (16)$$

The equation can express Gibbs' free energy (ΔG)[79]

$$\Delta G = -RT \ln K_{ads} \quad (17)$$

Arrhenius equation used to calculate the activation energy E_a (kJ mol^{-1}). The activation energy is the minimum energy required for a reaction to proceed.[80]

$$\ln k_2 = \ln A - \frac{E_a}{RT} \quad (18)$$

where k_2 is the pseudo-second-order rate constant at temperature T (K), A is the Arrhenius constant, E_a is the activation energy (kJ mol^{-1}), and R is the gas constant (8.314 J mol^{-1} K^{-1}). The activation energy can be calculated from the plot of $\ln k_2$ *versus* $1/T$.

Characterizations

The optical properties of the green-synthesized manganese (oxyhydr) oxide nanocomposite were measured using a JENWAY 6850 UV-vis spectrophotometer. The direct optical energy bandgap of the green-synthesized manganese (oxyhydr) oxides nanocomposite was calculated using Tauc's equation.[81]

$$(\alpha h\nu)^2 = B(h\nu - E_g) \quad (19)$$

where α is the absorption coefficient, (E_g) is the energy band gap, B is a constant which depends on the probability of transition, and $h\nu$ is the incident photon energy.

Debye–Scherrer equation.[82] It was used to calculate the crystallite size of green-synthesized manganese (oxyhydr) oxide nanocomposite.

$$D = \frac{0.9\lambda}{\beta \cos\theta} \quad (20)$$

where D is the crystallite size, 0.9 is the Scherrer constant, λ is the X-ray wavelength, which is equal to 1.54 Å, β is the full-width half maximum (FWHM), and θ is the Bragg's angle.

The structural properties of the green-synthesized manganese (oxyhydr) oxide nanocomposite were studied using a Philips PW1730 X-ray diffraction system in the 2θ range (10° to 80°) with CuKα = 1.54 Å.

The morphological properties of the green-synthesized manganese (oxyhydr) oxide nanocomposite were studied using the ZEISS Field Emission Scanning Electron Microscopy (FE-SEM) system, and its compositional properties were analyzed using EDX spectroscopy (FEI company, US). The N_2 adsorption–desorption test of the green-synthesized manganese (oxyhydr) oxide nanocomposite was conducted using a BELSORP II mini (Japan).

Results and discussion

Phytochemical screening of *Eriobotrya japonica* leaf extract

The results of the phytochemical tests of EJLE are shown in Table 2 and Fig. 4. The symbols + and − denote the presence and absence of bioactive compounds in the EJLE, respectively. The indication column summarizes the outcomes of the qualitative screening tests performed for these bioactive compounds.

FT-IR results

The FTIR spectra of the green synthesized manganese (oxyhydr) oxide nanocomposite and *Eriobotrya japonica* leaves extract were recorded in the range 400–4000 cm^{-1}, as shown in Fig. 5(a) and (b). From Fig. 5a, the peaks at 3398 and 3421 cm^{-1} corresponded to the O–H stretching and moisture in the samples.[83] The peak at 2424 cm^{-1} may be attributed to the (–CH_2–) symmetric stretching.[84] The sharp peak at 1786 cm^{-1}

Fig. 4 Phytochemical tests for *Eriobotrya japonica* leaf extract.

Table 2 Phytochemical analysis of *Eriobotrya japonica* leaf extract

Bioactive compound	Chemical test	Results	Indication	Ref.
Flavonoids	$Pb(CH_3COO)_2$	++	Yellow precipitation	51 and 52
Carbohydrates	Molisch test	+	Violet ring	53
Tannins	Braymer's test	+	Brownish-green	54–56
Alkaloids	Hager's test	−	No creamy white precipitate	57
Saponins	Foam test	+	Foam	58
Proteins and amino acid	Ninhydrin	−	No change in color	60
Phenolics	$Pb(CH_3COO)_2$	+	White precipitation	59

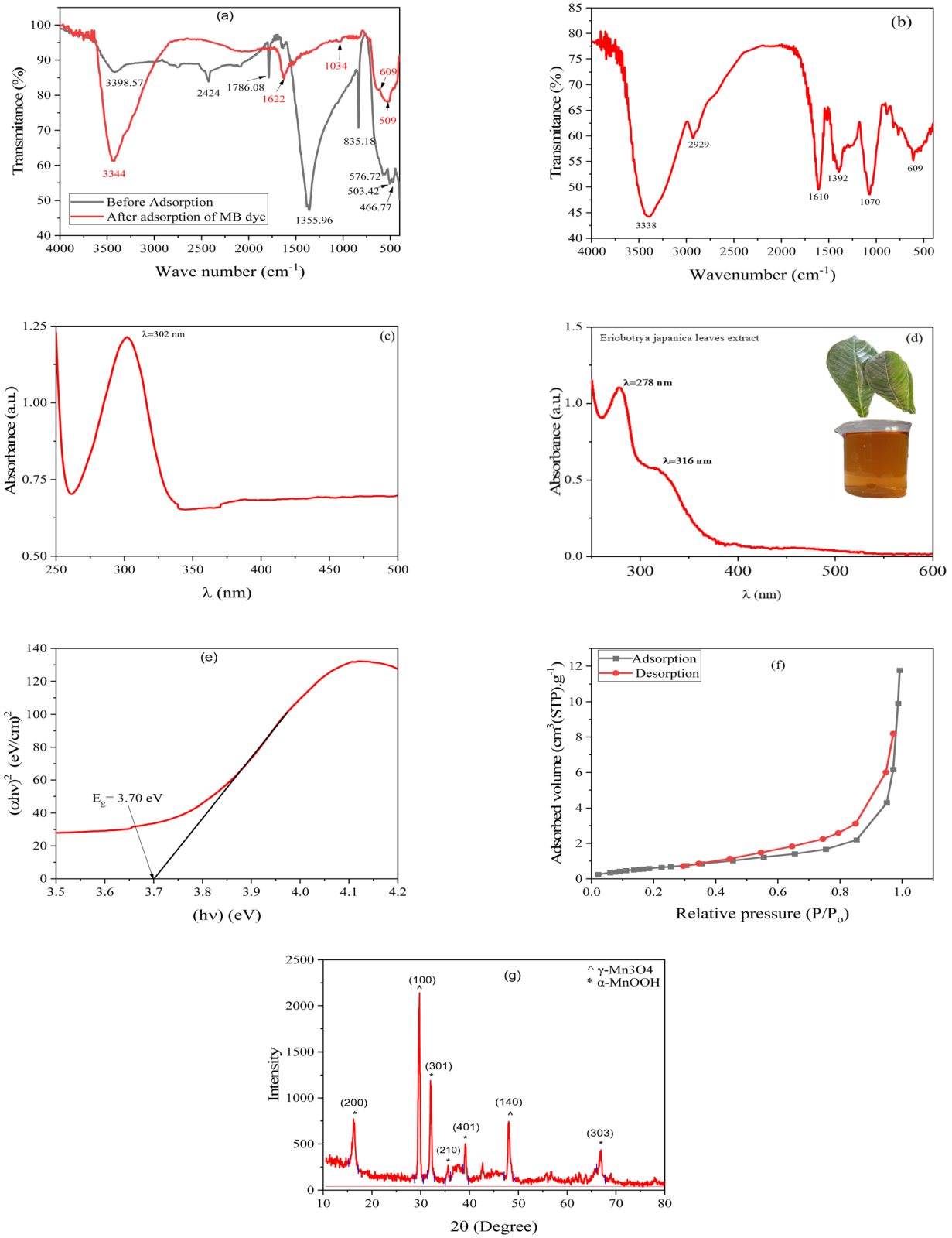

Fig. 5 (a) FT-IR spectra of manganese (oxyhydr) oxide nanocomposite before and after MB dye adsorption, (b) FT-IR spectra of *Eriobotrya japonica* leaf extract (EJLE), (c) absorbance spectra of the green-synthesized manganese (oxyhydr) oxide nanocomposite, (d) absorbance spectra of the *Eriobotrya japonica* leaf extract, (e) plots of $(\alpha h\nu)^2$ *versus* $h\nu$ of the manganese (oxyhydr) oxide nanocomposite, (f) N_2 adsorption–desorption isotherm of the green-synthesized manganese (oxyhydr) oxide nanocomposite, (g) XRD patterns of green-synthesized manganese (oxyhydr) oxide nanocomposite.

Table 3 XRD patterns of green-synthesized manganese (oxyhydr) oxide nanocomposite

No.	Diffracted peaks 2θ	Planes	Phase
1	16.3201	(200)	Groutite
2	29.6749	(100)	Mn_3O_4
3	32.0706	(301)	Groutite
4	35.5736	(210)	Groutite
5	39.1918	(401)	Groutite
6	47.9899	(140)	Mn_3O_4
7	66.8312	(303)	Groutite

corresponds to the (C=O) stretching.[50] The peaks (1355 and 835 cm^{-1}) can be attributed to the NO_3^-.[85] The peaks at 466, 503, and 576 cm^{-1} are related to the Mn–O stretching vibration of manganese (oxyhydr) oxide nanocomposite.

The FTIR of the *Eriobotrya japonica* leaf extract can be seen in Fig. 5b. The strong band at 3338 cm^{-1} may be attributed to the O–H and N–H stretching vibration. The peak at 2929 cm^{-1} corresponded to the stretching vibration of the C–H.[86] The band 1610 cm^{-1} is attributed to the C=C stretching vibration. The peak at 1392 cm^{-1} could be related to the bending of the C–H in $-CH_3$. The band at 1070 cm^{-1} corresponds to the C–O or C–H stretching vibration. The band at 609 cm^{-1} could have corresponded to the C–H of aromatic or aliphatic carbon.[87]

Optical properties

The UV-vis absorption spectra of the *Eriobotrya japonica* leaf extract and the green-synthesized manganese (oxyhydr) oxide nanocomposite were recorded in the wavelength range of 250–600 nm, as illustrated in Fig. 5c and d. The plant extract exhibited two characteristic absorption bands at 278 nm and 316 nm, attributed to surface plasmon resonance, confirming the presence of phytochemical constituents, as shown in Fig. 5d. The absorption region between 250 and 320 nm is associated with $n \rightarrow \pi^*$ transitions of functional groups such as O–H and COOH present in the extract, highlighting the role of phytochemicals as effective reducing and stabilizing agents.[88,89] However, Fig. 5c presents the absorption peaks of the green synthesized manganese (oxyhydr) oxide nanocomposite. The green-synthesized manganese (oxyhydr) oxide nanocomposite exhibits an absorption peak at 302 nm. The single and sharp absorption peak of the green-synthesized manganese (oxyhydr) oxide nanocomposite indicates the uniform distribution and nanosized particles.[90]

A plot of $(\alpha h\nu)^2$ *versus* $h\nu$ is shown in Fig. 5e and was used to determine the energy gap of the green-synthesized manganese (oxyhydr) oxides. The linear segment of the curves is extended to the $h\nu$ axis to ascertain the energy bandgap, which is 3.70 eV.

Structural properties

The XRD results of the green-synthesized manganese (oxyhydr) oxide nanocomposite are shown in Fig. 5g, and Table 3 revealed that the diffracted patterns match with the marokite (γ-Mn_3O_4) peaks indexed in the (JCPDS card no. 96-900-1303) with the orthorhombic crystal structure space group (*Pbcm*) and groutite (α-MnOOH) (JCPDS card no. 96-901-1547) with the orthorhombic crystal structure and space group (*Pnma*).

The high intensity is an indication of good crystallinity of the (γ-Mn_3O_4) and (α-MnOOH) nanostructures in the nanocomposite. The crystallite size was calculated to be 30.83 nm.

N_2 adsorption–desorption isotherm of green-synthesized manganese (oxyhydr) oxide nanocomposite

The porosity of green-synthesized manganese (oxyhydr) oxide nanocomposite (Fig. 5f) was acquired by measuring N_2 adsorption–desorption isotherms at 77 K. The adsorbed quantity increased gradually at low pressures and sharply at high pressures, exhibiting a type-IV isotherm and a type-H3 hysteresis loop (defined by IUPAC) at a relative pressure of nearly $P/P_o = 0.5$–1, indicating the presence of mesopores in the green-synthesized manganese (oxyhydr) oxide nanocomposite. Brunauer–Emmett–Teller (BET) isotherm was employed to analyze the porosity parameters. The results showed that the BET specific surface area of the green-synthesized manganese (oxyhydr) oxide nanocomposite is 2.5808 $m^2\ g^{-1}$, total pore volume ($P/P_o = 0.990$) is 0.017075 $cm^3\ g^{-1}$, and mean pore diameter is 26.464 nm.

Morphological properties

The FESEM micrographs shown in Fig. 6a reveal that the green-synthesized manganese (oxyhydr) oxide nanocomposite, composed of γ-Mn_3O_4 and α-MnOOH phases, exhibits two distinct nanostructures: nanoparticles and nanorods. Crystal faces with higher surface energy tend to grow more rapidly, leading to the formation of smaller facets that may eventually disappear, whereas faces with lower surface energy grow at a slower rate and are more likely to be preserved in the final morphology.[91] The particle sizes calculated from the FE-SEM images were found to be 37.72 nm for the green-synthesized manganese (oxyhydr) oxide nanocomposite. The particle sized calculated from the FE-SEM image are bigger than those calculated from the XRD data this can be attributed due to their higher surface area and high surface-to-volume ratio, small particles are more likely to interact with their neighbouring surface atoms to create agglomerations of a particle because they have more surface atoms and, thus, more dangling bonds and it is essential to remember that the crystallite size (D) may not always correspond to the particle size; rather, it represents the size of a coherently diffracting domain.[92]

Compositional properties

The energy dispersive X-ray technique was utilized to study the elemental composition of the green-synthesized manganese (oxyhydr) oxide nanocomposite, as shown in Fig. 6c, which confirms the predominant presence of the peaks of the Mn and O, with the presence of unidentified peaks. The EDS results support the XRD results, indicating good crystallinity of the products. From Table 4 it can be seen that the weight and atomic ratio percentage of oxygen are dominant. The atomic ratio of green synthesized manganese (oxyhydr) oxide

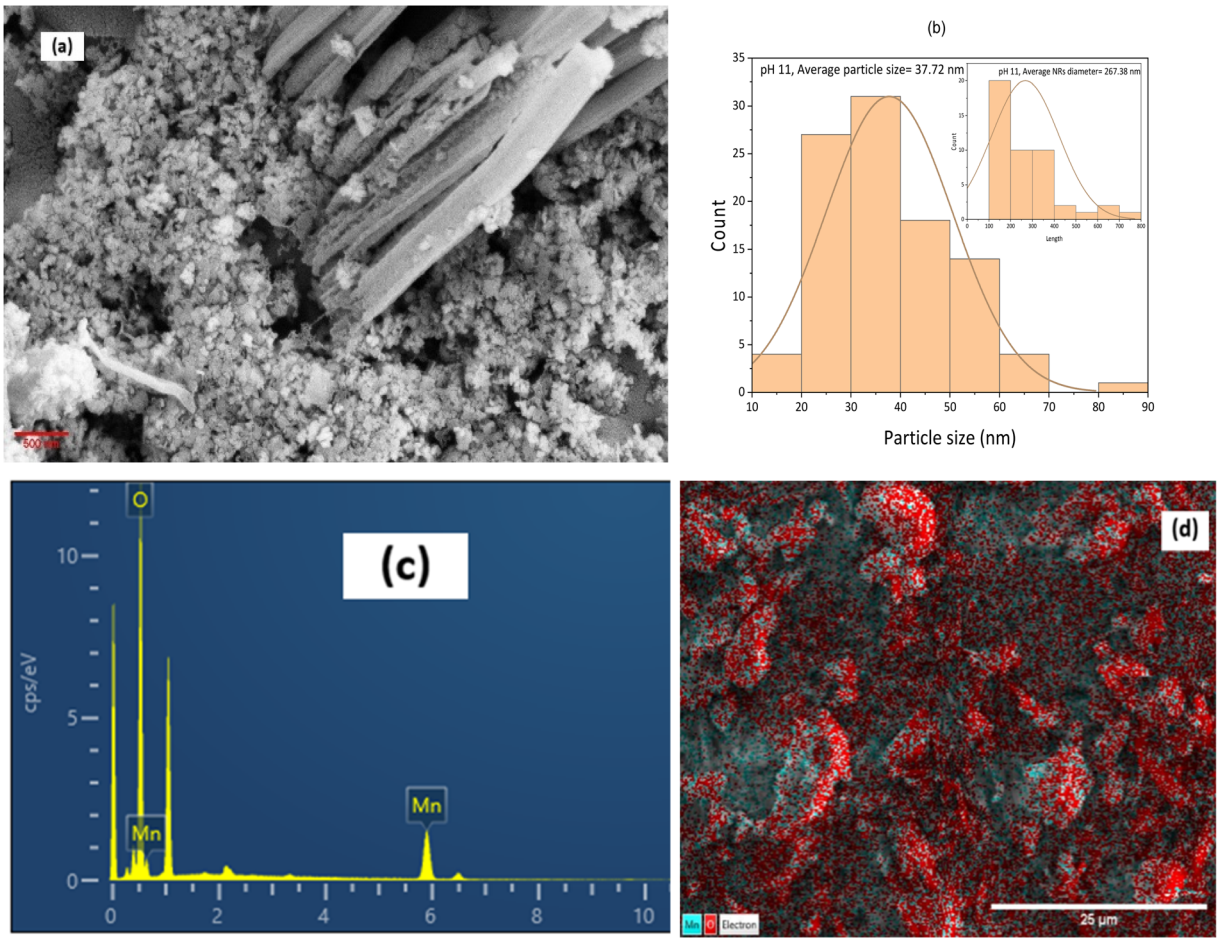

Fig. 6 (a) FESEM images, (b) particle size distribution, (c) EDS, and (d) mapping of the green-synthesized manganese (oxyhydr) oxide nanocomposite.

Table 4 Compositional weight and atomic ratio of Mn and O for green-synthesized manganese (oxyhydr) oxide nanocomposite

Weight%		Atomic%	
Mn	O	Mn	O
34.62	65.38	13.36	86.64

nanocomposite is smaller than 3 : 4. This can be evidence that the green synthesized manganese (oxyhydr) oxide nanocomposite consists of a composite of manganese (oxyhydr) oxides (γ-Mn_3O_4) and (α-MnOOH).[93]

Adsorption activity of the green-synthesized manganese (oxyhydr) oxide nanocomposite

Effect of the initial pH of the MB dye solution. Solution pH plays a pivotal role in governing the interfacial interactions between the adsorbate and adsorbent. It significantly influences the adsorption performance by regulating the surface charge of the adsorbent through protonation and deprotonation of its functional groups, thereby affecting the overall adsorption behavior.[94]

Fig. 7a depicts the influence of solution pH on the adsorption of methyl blue dye. The results demonstrate a clear enhancement in both adsorption capacity and removal efficiency with increasing pH. Under strongly acidic conditions, the high concentration of H^+ ions leads to competitive interactions with methyl blue molecules and partial protonation of surface functional groups, which weakens the affinity between the dye and the manganese (oxyhydr) oxide nanocomposite. As the pH rises, this competitive effect diminishes, and the availability of surface functional groups such as $-NH_2$, –OH, and –COOH increases alongside a reduction in H^+ concentration and a corresponding increase in OH^- ions. These conditions promote stronger interactions between the adsorbent surface and dye molecules, resulting in improved adsorption performance.[95]

Effect of the adsorbent dosage. The effect of adsorbent dosage on the adsorption performance was investigated by varying the amount of manganese (oxyhydr) oxide nanoparticles while maintaining constant experimental conditions, including an initial methyl blue concentration of 133.33 mg L^{-1}, solution pH of 10, and temperature of 283 K. As illustrated in Fig. 7b, the removal efficiency of methyl blue increased markedly from 76% to 91.95% with increasing adsorbent dosage. This improvement is attributed to the higher availability of surface area and an

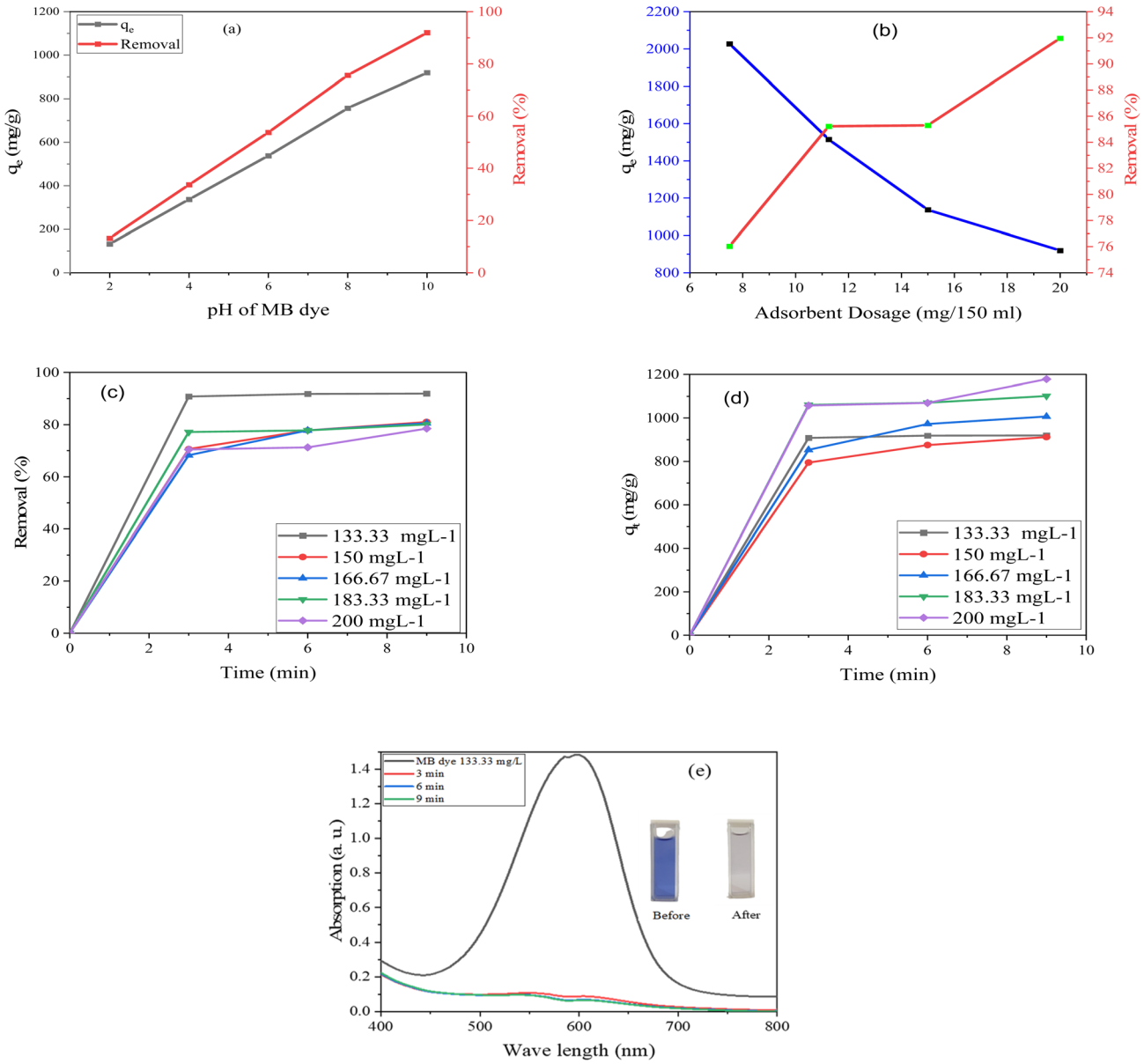

Fig. 7 (a) Effect of the pH value of the MB dye, (b) effect of adsorbent dose, (c) effect of the initial MB dye concentration on the removal percentage, (d) effect of the initial MB dye concentration on the on q_e, (e) absorbance spectra of the adsorption of MB dye onto green-synthesized manganese (oxyhydr) oxide nanocomposite at dye concentration (133.33 mg L^{-1}), pH 10, adsorbent dosage NPs dosage 20 mg/150 mL, temperature 283 K.

increased number of active adsorption sites provided by the greater quantity of manganese (oxyhydr) oxide nanocomposite, which enhances dye uptake.[96] The adsorption capacity exhibited an almost linear decline from 2027.4 mg g^{-1} to 919.54 mg g^{-1} as the adsorbent dosage increased from 7.5 to 20 mg/150 mL. At lower dosages, the limited number of adsorbent particles provides fewer available active sites, allowing each particle to bind a larger amount of dye and resulting in a higher equilibrium adsorption capacity (q_e). In contrast, increasing the adsorbent dosage introduces a greater number of active sites, causing the dye molecules to be distributed across more particles. Consequently, a portion of the adsorption sites remains unoccupied, leading to a decrease in the amount of dye adsorbed per unit mass of adsorbent.[97]

Overall, increasing the adsorbent dosage enhances the available surface area and number of active sites, resulting in improved adsorption efficiency. However, the adsorption capacity per unit mass decreases as a consequence of the presence of unoccupied active sites at higher dosages.

Effect of the MB dye concentration. Fig. 7c and d represent the adsorption percentage rate and adsorption capacity of the methyl blue dye onto the green-synthesized manganese (oxyhydr) oxide nanocomposite adsorbent for different concentrations of the MB dye. Fig. 7c illustrates that a high amount of the MB dye, about 70 to 90%, is adsorbed in the first 3 minutes

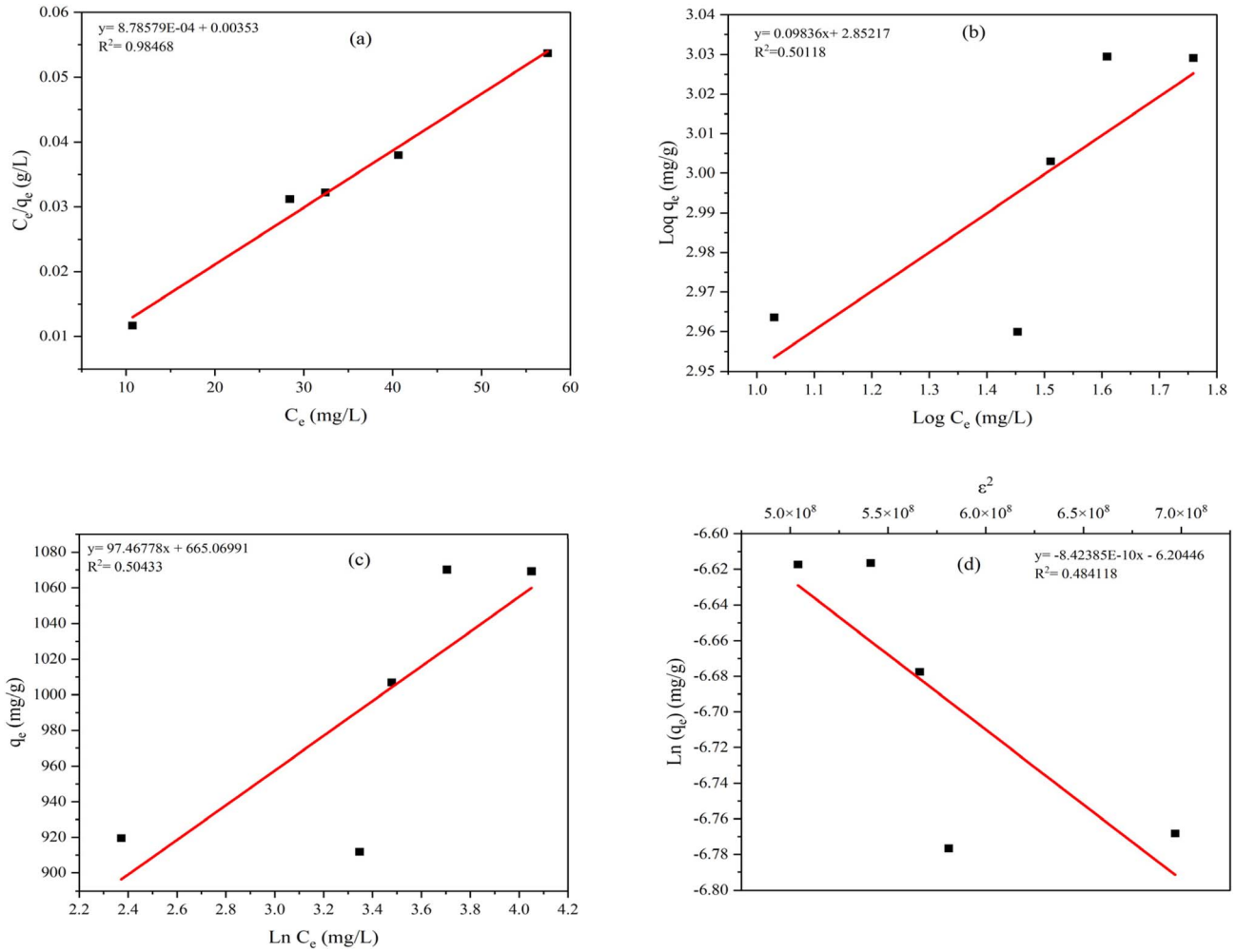

Fig. 8 Adsorption isotherms: (a) Langmuir isotherm, (b) Freundlich isotherm, (c) Temkin isotherm, and (d) Dubinin–Radushkevich (D–R) isotherm.

for all concentrations; after that, it slightly increases. Also, Fig. 7d shows that the adsorption capacity sharply increases in the first 3 minutes. This can be due to the availability of the active sites after the most active sites are occupied by the dye molecules, the removal percentage, and the adsorption capacity fairly change.[2] The adsorption mechanism proceeds in two distinct stages. Initially, methyl blue dye molecules are rapidly transported from the solution to the external surface of the adsorbent within the first 3 minutes, corresponding to an external diffusion–controlled step. Subsequently, the adsorption process is governed by the migration of the dye molecules from the adsorbent surface into its internal pore structure, representing the intraparticle diffusion stage.[98] As the initial concentration increased from 133.33 mg L^{-1} to 200 mg L^{-1}, the removal percentage decreased from 91.95% to 78.52%, while the adsorption capacity increased from 919.54 mg g^{-1} to 1177.85 mg g^{-1}. The adsorbent surface becomes increasingly saturated and inaccessible as the initial concentration of the MB dye rises, resulting in a steady decline in the removal rate.[99,100]

Adsorption isotherms result of the green-synthesized manganese (oxyhydr) oxide nanocomposite

The equilibrium adsorption behavior of methyl blue (MB) onto the green-synthesized manganese (oxyhydr) oxide nanocomposite was evaluated using Langmuir, Freundlich, Temkin, and Dubinin–Radushkevich (D–R) isotherm models, as shown in Fig. 8 and Table 5. Among these, the Langmuir model exhibited the best fit to the experimental data, as evidenced by the high correlation coefficient (R^2 = 0.9846), indicating monolayer adsorption on a homogeneous surface with finite and energetically equivalent active sites. The remarkably high maximum adsorption capacity (q_{max} = 1138.2 mg g^{-1}) highlights the strong affinity of MB molecules toward the manganese (oxyhydr) oxide surface. Furthermore, the dimensionless separation factor (R_L = 0.0199–0.029) lies between 0 and 1, confirming that the adsorption process is highly favorable under the studied conditions.[76,100]

In contrast, the Freundlich model showed a poor correlation (R^2 = 0.5), suggesting that multilayer adsorption on a heterogeneous surface is not the dominant mechanism, despite the high

Table 5 Adsorption isotherms parameters

Isotherms	Parameters	Values
Langmuir isotherm	q_{max} (mg g^{-1})	1138.2
	K_L (L mg^{-1})	0.2488
	R_L	0.019–0.029
	R^2	0.9846
Freundlich isotherm	$1/n$	0.098
	n (mg g^{-1})	10.16
	K_f (mg g^{-1})	711.49
	R^2	0.5
Temkin isotherm	A_T (L g^{-1})	919.18
	b_t (J mol^{-1})	24.13
	B (L g^{-1})	97.46
	R^2	0.5
Dubinin–Radushkevich (D–R) isotherm	q_{DR} (mg g^{-1})	0.002
	K_{DR} (mol^2 kJ^{-2})	8.42×10^{-10}
	E (kJ mol^{-1})	24.362
	R^2	0.484

Freundlich constant (K_f = 711.49 mg g^{-1}) and the value of $1/n$ (0.098), which still implies favorable adsorption intensity.[101,102] Similarly, the Temkin model yielded a low R^2 value (0.5), indicating limited applicability; however, the Temkin constant related to adsorption heat (B = 97.46 J mol^{-1}) suggests notable adsorbate–adsorbent interactions. The D–R isotherm also poorly described the system (R^2 = 0.484). Overall, the isotherm analysis confirms that MB adsorption onto green-synthesized manganese (oxyhydr) oxide nanocomposite is a favorable, monolayer, and predominantly chemisorption process with exceptionally high adsorption capacity, underscoring its potential as an efficient adsorbent for dye-contaminated wastewater.

Table 6 represents the maximum adsorption capacity of the methyl blue dye onto the different adsorbents. This study's maximum adsorption capacity shows competitive performance with literature works, which is 1138.2 mg. This can be attributed to the presence of active sites on the green-synthesized nanoparticles.

Adsorption kinetics results of the green-synthesized manganese (oxyhydr) oxide nanocomposite

The pseudo-first-order and pseudo-second-order kinetics models were employed to evaluate the adsorption rate of different MB dye concentrations (133.33, 150, 166.67, 183.33, and 200 mg L^{-1}). As illustrated and tabulated in Fig. 9, and Table 7 the kinetic parameters for methyl blue adsorption onto the green-synthesized manganese (oxyhydr) oxide nanocomposite reveal clear differences in the suitability of the applied models. The pseudo-first-order model shows relatively low correlation coefficients (R^2 = 0.5957–0.9993) and calculated adsorption capacities ($q_{e,cal}$) that deviate substantially from the experimental values ($q_{e,exp}$), indicating that this model does not adequately describe the adsorption behavior over the studied concentration range. In contrast, the pseudo-second-order model shows excellent agreement with the experimental data, with very high correlation coefficients (R^2 = 0.9841–0.99999) and $q_{e,cal}$ values that closely match $q_{e,exp}$ across all initial dye concentrations. This strong conformity suggests that the adsorption process is predominantly governed by chemisorption involving valence forces or electron sharing between the dye molecules and active sites on the nanocomposite surface.[112,113]

Fig. 9c and Table 7 represent the intraparticle diffusion kinetic model. Furthermore, the intraparticle diffusion model yields lower R^2 values (0.5293–0.96) and nonzero intercepts (C_{int}), implying that intraparticle diffusion is not the sole rate-controlling step. Instead, the adsorption kinetics are influenced by multiple mechanisms, including rapid external surface adsorption followed by slower diffusion of dye molecules into the internal pores of the adsorbent.[2,114]

Overall, the kinetic analysis confirms that the adsorption of methyl blue onto the green-synthesized manganese (oxyhydr) oxide nanocomposite is best described by the pseudo-second-order model, with a multistep adsorption mechanism.

Thermodynamic parameters

Based on the thermodynamic parameters calculated from Fig. 10a and tabulated in Table 8. The adsorption behavior of methyl blue (MB) dye onto the green-synthesized manganese (oxyhydr) oxide nanocomposite can be interpreted as follows:

The negative values of Gibbs free energy change ($\Delta G°$) at all investigated temperatures (−10.47 to −7.22 kJ mol^{-1}) confirm that the adsorption of MB is a spontaneous process. The gradual increase in $\Delta G°$ (becoming less negative) with

Table 6 Adsorption capacity of MB dye by various adsorbents

Adsorbents	q_e mg g^{-1}	Ref.
Mespilus germanica L. fruits seed biochar (MGLfsB)	11.148	103
Nanomagnetic *Mespilus germanica* L. fruit seed biochar (nM-MGLfsB)	13.089	103
Amino-functionalized zeolitic imidazole framework-8 (ZIF-8/NH_2 nanoparticles)	537.4	104
Activated carbon eggshell (ACE)	45.23	105
$Na_2Al_2B_2O_7$	2000	106
Copper-based triazolate MOFs (CuTz-1-Py)	352.3	107
Banana leaves powder (BLP)	84.24	108
Activated carbon banana leaves powder (AC-BLP)	386	108
Crosslinked chitosan-citrate/SnO_2 nanoparticles (CTN-CT/SnO_2)	511.92	109
CMBLP	118.24	110
Pinus brutia biochar (PBB)	66.667	111
Nano-magnetic *Pinus brutia* biochar (nM-PBB)	107.527	111
Mn (oxyhyrd) oxide nanocomposite of (Mn_3O_4, MnOOH)	***1138.2***	***This study***

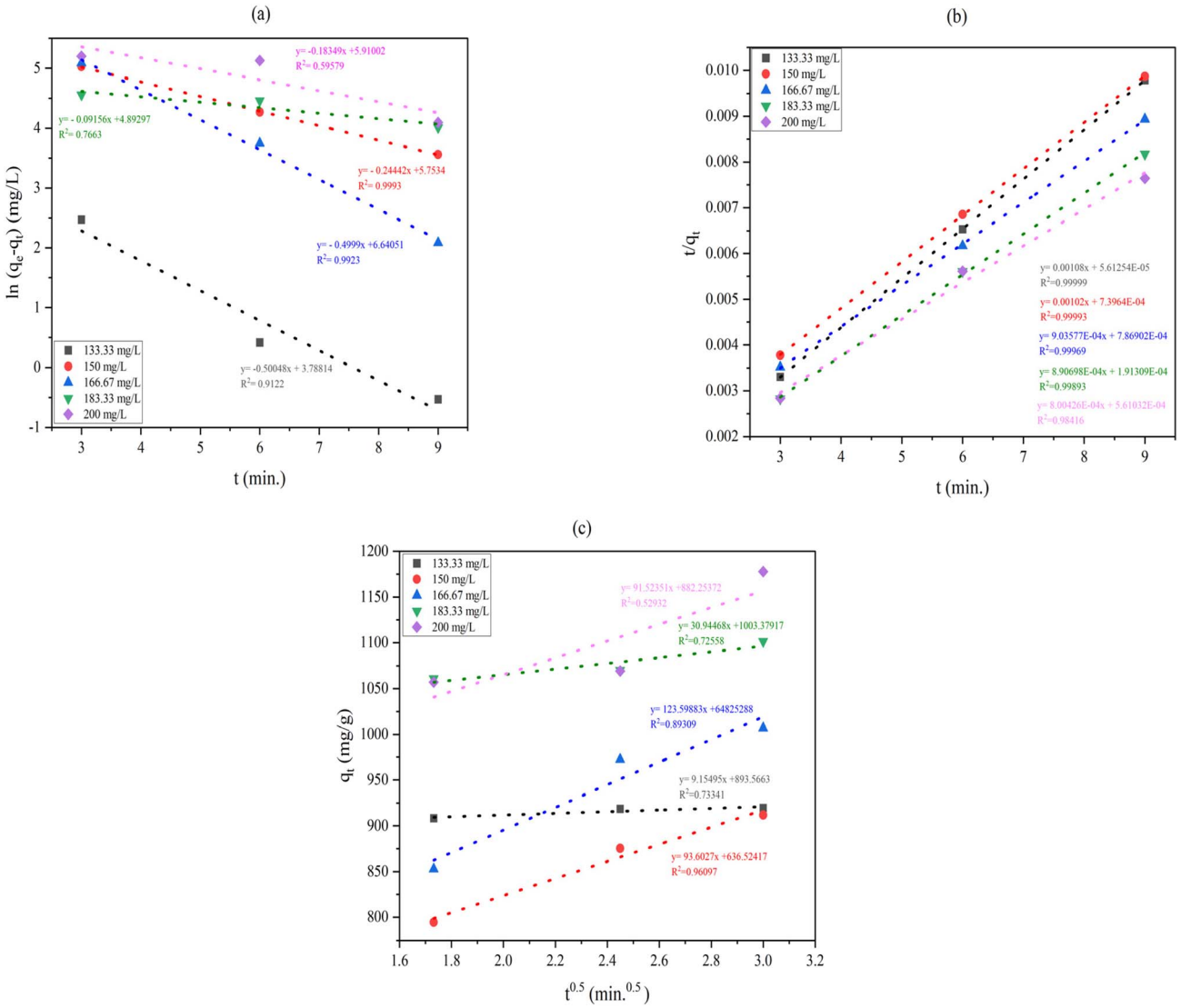

Fig. 9 Adsorption kinetics models plot (a) pseudo-first order, (b) pseudo-second order, and (c) the intraparticle diffusion model.

increasing temperature suggests that the feasibility of adsorption slightly decreases at higher temperatures, indicating that lower temperatures are more favorable for MB uptake. The negative enthalpy change ($\Delta H^\circ = -46.39$ kJ mol^{-1}) demonstrates that the adsorption process is exothermic, chemisorption, and implies strong interactions between MB molecules and the surface of the manganese (oxyhydr) oxide nanocomposite.[115] Moreover, the negative entropy change ($\Delta S^\circ = -126.54$ J mol^{-1} K^{-1}) reflects a decrease in randomness at the solid–solution interface during adsorption, which can be

Table 7 Kinetic parameters for methyl blue dye adsorption onto the green-synthesized manganese (oxyhydr) oxide nanocomposite at various MB concentrations

	Pseudo-first order			Pseudo-second order			Intraparticle diffusion			
Methyl blue dye concentration (mg L^{-1})	K_1 (min^{-1})	q_e (mg g^{-1})	R^2	K_2 (g mg^{-1} min^{-1})	q_e (mg g^{-1})	R^2	K_{IPD} (mg g^{-1} min$^{-0.5}$)	C_{int}	R^2	q_e (exp.)
133.33	0.5	44.17	0.9122	0.02	925.22	0.99999	9.155	893.56	0.7334	919.54
150	0.2444	315.26	0.9993	0.0014	980.39	0.99993	93.6	636.52	0.96	911.86
166.67	0.4999	765.48	0.9923	0.001	1106.71	0.9997	123.59	648.25	0.893	1006.88
183.33	0.09156	133.34	0.7663	0.0041	1122.76	0.9989	30.94	1003.3	0.7255	1101.32
200	0.1834	368.71	0.5957	0.0011	1249.33	0.9841	91.52	882.25	0.5293	1177.65

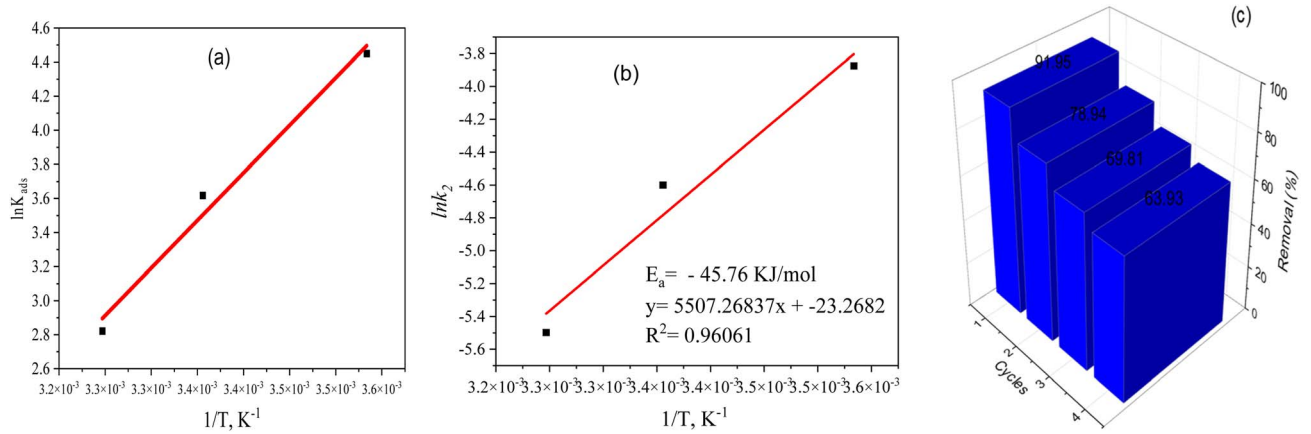

Fig. 10 (a) Plot of ln K_{ads} *versus* 1/*T* of the adsorption process of methyl blue dye onto the green-synthesized manganese (oxyhydr) oxides nanocomposite, (b) plot ln k_2 *versus* 1/*T*, (c) reusability of green-synthesized manganese (oxyhydr) oxide nanocomposite.

Table 8 Thermodynamic parameters of the adsorption process of methyl blue dye onto the green-synthesized manganese (oxyhydr) oxide nanocomposite

T (K)	Δ*G* (kJ mol^{-1})	Δ*H* (kJ mol^{-1})	Δ*S* (J mol^{-1} K^{-1})	R^2
283	−10.47	−46.39	−126.54	0.9687
298	−8.96			
308	−7.22			

attributed to the orderly attachment of MB molecules onto the adsorbent surface.[116–118]

The high correlation coefficient ($R^2 = 0.9687$) indicates good linearity of the thermodynamic model, confirming the reliability of the calculated parameters. Collectively, these results suggest that MB adsorption onto the manganese (oxyhydr) oxide nanocomposite is spontaneous, exothermic, and accompanied by increased structural ordering at the adsorbent–adsorbate interface.

As shown in Fig. 10b, the calculated activation energy ($E_a = -45.76$ kJ mol^{-1}) indicates that the adsorption of methyl blue dye onto the green-synthesized manganese (oxyhydr) oxide nanocomposite is mainly governed by a chemisorption mechanism. In general, activation energy values within the range of 5–40 kJ mol^{-1} are typically attributed to physisorption, whereas higher values (approximately 40–800 kJ mol^{-1}) are associated with chemisorption processes.[119] It should be noted that, in certain adsorption systems, the adsorption rate may decrease as temperature increases. Under such conditions, the rate constant can still be described by the Arrhenius equation, which may yield a negative activation energy value.[120] The negative E_a obtained in this study indicates that the adsorption process is exothermic in nature. This observation is consistent with the kinetic results, which demonstrate that the adsorption behavior follows the pseudo-second-order kinetic model, suggesting that chemical interactions play a significant role in the adsorption mechanism.

Adsorption mechanism

The FTIR spectra of the green-synthesized manganese (oxyhydr) oxide nanocomposite before and after adsorption of methyl blue (MB) Fig. 5a show noticeable changes in the positions and intensities of several characteristic peaks, indicating the participation of surface functional groups in the adsorption process.[108] In particular, the –OH, –NH, C–O, C–N, and Pb–O groups were actively involved in the interaction with MB molecules.[121] The broad O–H stretching vibration observed at 3398 cm^{-1} in the green-synthesized manganese (oxyhydr) oxide nanocomposite shifts to a lower wavenumber (3344 cm^{-1}) after MB adsorption. This red shift suggests the formation of hydrogen bonding interactions between MB molecules and hydroxyl groups on the surface of the green-synthesized manganese (oxyhydr) oxide nanocomposite.

Furthermore, a new absorption band appears at 1622 cm^{-1} in the MB-loaded nanocomposite, which is attributed to the deformation vibration of –NH_2 groups derived from the dye molecules.[110] Another new band at 1034 cm^{-1} corresponds to the sulfonate (–SO_3^-) functional group of MB, providing clear evidence for the successful adsorption of the dye onto the nanocomposite surface.[122] In addition, slight shifts and reductions in the intensity of the Mn–O stretching vibration bands were observed after adsorption, indicating interactions between the dye molecules and Mn–O surface sites within the nanocomposite lattice. Collectively, these spectral changes confirm the effective adsorption of MB onto the green-synthesized manganese (oxyhydr) oxide nanocomposite.

The adsorption mechanism appears to be governed by multiple interactions, including hydrogen bonding, electrostatic attraction, n–π interactions, and pore filling, reflecting the complex nature of the adsorption behavior. Hydrogen bonding plays a significant role through interactions between hydrogen atoms on surface hydroxyl groups of green-synthesized manganese (oxyhydr) oxide nanocomposite and oxygen- and nitrogen-containing functional groups of MB dye molecules. The π bond of the benzene ring on MB can generate a specific interaction with metals. MB with rich benzene rings

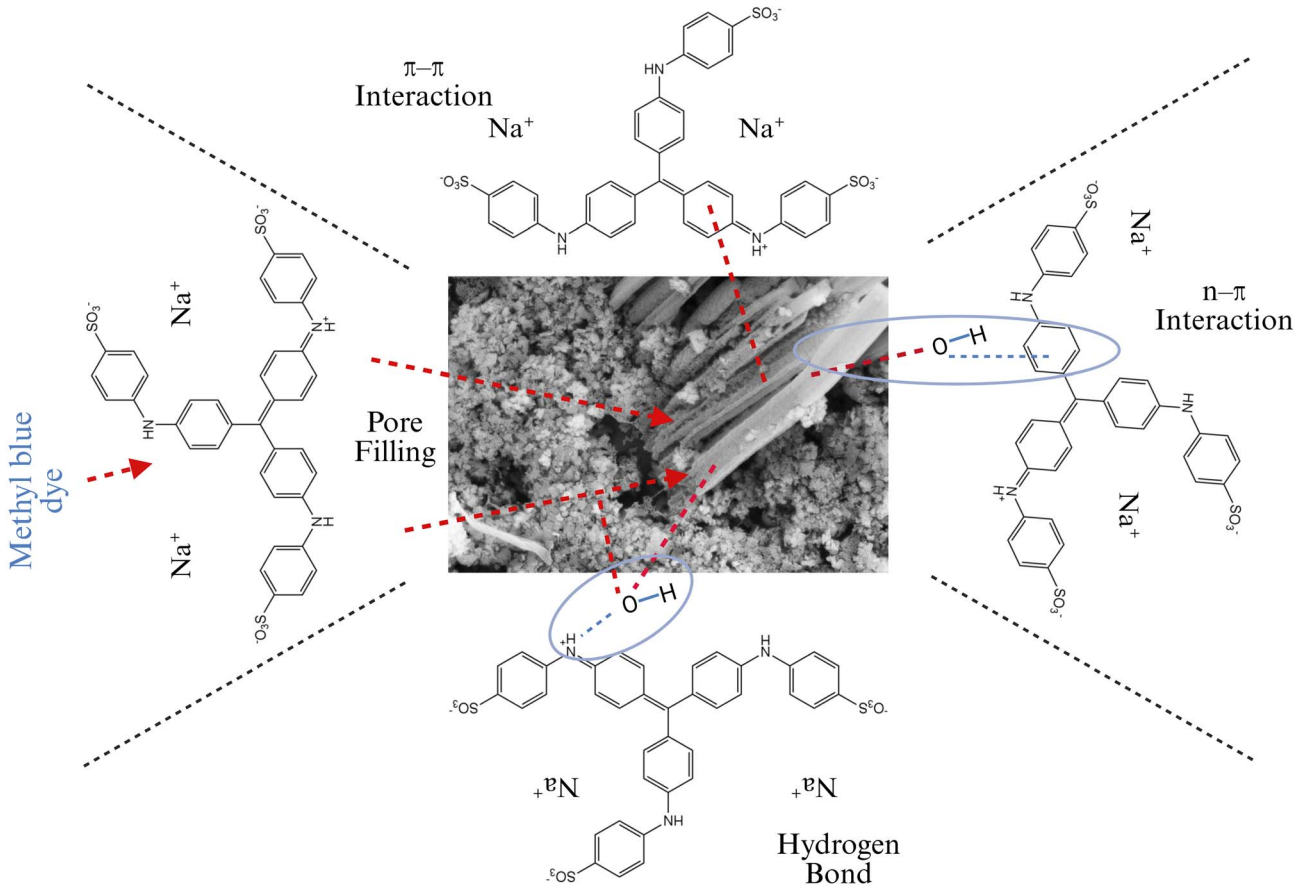

Fig. 11 Schematic representation of the adsorption of methyl blue dye onto the green-synthesized manganese (oxyhydr) oxide nanocomposite.

can generate π-interactions with manganese.[123,124] The schematic of the MB adsorption on the green-synthesized manganese (oxyhydr) oxide nanocomposite can be seen in Fig. 11.

In addition, the fitting of the experimental data to the Langmuir isotherm model, the pseudo-second-order (PSO) kinetic model, the magnitude of the enthalpy change, and the calculated activation energy values collectively indicate that the adsorption of MB onto green-synthesized manganese (oxyhydr) oxide nanocomposite is predominantly controlled by chemisorption. These results suggest that chemical interactions constitute the primary adsorption mechanism, although a minor contribution from physisorption cannot be excluded.

Reusability of the green-synthesized manganese (oxyhydr) oxide nanocomposite

The reusability performance of the green-synthesized manganese (oxyhydr) oxide nanocomposite was evaluated through consecutive adsorption–desorption cycles for methyl blue removal under optimized conditions (pH 10, initial dye concentration 133.33 mg L^{-1}, adsorbent dose 20 mg/150 mL, temperature 283 K, and contact time 9 min). After each adsorption run, the used adsorbent was regenerated by thoroughly rinsing it with ethanol, followed by distilled water, to remove the dye molecules bound to its surface. As illustrated in Fig. 10c, the adsorption efficiency notably declined with increasing number of reuse cycles. The first cycle exhibited the highest removal efficiency. A moderate decrease was observed in subsequent cycles, likely due to partial blockage of adsorption sites, incomplete desorption of dye molecules, and possible structural or surface chemical changes in the nanocomposite during regeneration. Nevertheless, the adsorbent retained a considerable fraction of its initial adsorption capacity even after multiple cycles, indicating acceptable regeneration potential. These results demonstrate that the green-synthesized manganese (oxyhydr) oxide nanocomposite is a reusable and economically viable adsorbent for methyl blue removal from aqueous solutions, supporting its applicability in practical wastewater treatment processes.

Conclusion

The treatment of contaminated water, particularly the removal of dyes and heavy metals, remains a critical environmental challenge, with adsorption emerging as an effective and economical solution. In this study, manganese (oxyhydr) oxide nanocomposite, namely marokite (γ-Mn_3O_4) and groutite (α-MnOOH), were successfully synthesized *via* an environmentally friendly green route using *Eriobotrya japonica* leaf extract. Optical, structural, and morphological characterizations confirmed the formation of pure manganese (oxyhydr) oxides composed of nanoparticles and nanorods.

The green-synthesized manganese (oxyhydr) oxide nanocomposite exhibited good adsorption performance toward methyl blue dye. Adsorption equilibrium and kinetic analyses revealed that the process follows the Langmuir isotherm and pseudo-second-order kinetic model, indicating a monolayer chemisorption mechanism. Thermodynamic results demonstrated that the adsorption process is spontaneous and favorable. Moreover, the nanocomposite showed good reusability, retaining a substantial fraction of its adsorption capacity after multiple cycles, which reflects its stability and regeneration potential. The enhanced adsorption efficiency is attributed to phytochemicals in the plant extract, which play a key role in tailoring the nanomaterials' structural and surface properties. Overall, the green-synthesis technique provides an efficient and sustainable approach for producing manganese (oxyhydr) oxides with good potential for practical wastewater treatment applications.

Author contributions

Conceptualization, Raghad Yousif Mohammed; methodology, Raghad Yousif Mohammed; software, Honar Salah Ahmed; validation, Raghad Yousif Mohammed and Honar Salah Ahmed; formal analysis, Raghad Yousif Mohammed; investigation, Raghad Yousif Mohammed; resources, Raghad Yousif Mohammed; data curation, Honar Salah Ahmed; writing – original draft preparation, Honar Salah Ahmed; writing – review and editing, Raghad Yousif Mohammed.; visualization, Raghad Yousif Mohammed, and Honar Salah Ahmed; supervision, Raghad Yousif Mohammed; project administration, Raghad Yousif Mohammed all authors have read and agreed to the published version of the manuscript.

Conflicts of interest

The authors have no competing interests to declare that are relevant to the content of this article.

Data availability

The data were analyzed and used in this study are available upon a reasonable request from the corresponding author.

Acknowledgements

The authors would like to express their gratitude to the Ministry of Higher Education and Scientific Research in the Kurdistan Region and the University of Duhok for their support.

References

1 F. T. Alshorifi, S. L. Ali and R. S. Salama, *J. Inorg. Organomet. Polym. Mater.*, 2022, **32**, 3765–3776.
2 N. Hasani, T. Selimi, A. Mele, V. Thaçi, J. Halili, A. Berisha and M. Sadiku, *Molecules*, 2022, **27**, 1856.
3 B. Mu, L. Liu, W. Li and Y. Yang, *J. Environ. Manage.*, 2019, **239**, 271–278.
4 K. Azam, R. Raza, N. Shezad, M. Shabir, W. Yang, N. Ahmad, I. Shafiq, P. Akhter, A. Razzaq and M. Hussain, *J. Environ. Chem. Eng.*, 2020, **8**, 104220.
5 F. B. Loulic, R. H. S. M. Shirazi, M. Miralinaghi, H. A. Panahi and E. Moniri, *Microporous Mesoporous Mater.*, 2023, **356**, 112567.
6 M. M. Youssif, H. G. El-Attar, V. Hessel and M. Wojnicki, *Materials*, 2024, **17**, 5141.
7 N. Ghosh, S. Das, G. Biswas and P. K. Haldar, *Water Sci. Technol.*, 2022, **85**, 3370–3395.
8 I. Hussain, Y. Li, J. Qi, J. Li and L. Wang, *J. Environ. Manage.*, 2018, **215**, 123–131.
9 A. A. Yaqoob, H. Ahmad, T. Parveen, A. Ahmad, M. Oves, I. M. Ismail, H. A. Qari, K. Umar and M. N. Mohamad Ibrahim, *Front. Chem.*, 2020, **8**, 341.
10 S. J. Nadaf, N. R. Jadhav, H. S. Naikwadi, P. L. Savekar, I. D. Sapkal, M. M. Kambli and I. A. Desai, *OpenNano*, 2022, 100076.
11 S. M. Webb, B. Tebo and J. Bargar, *Am. Mineral.*, 2005, **90**, 1342–1357.
12 Z. Wu, B. Lanson, X. Feng, H. Yin, Z. Qin, X. Wang, W. Tan, Z. Chen, W. Wen and F. Liu, *Geochim. Cosmochim. Acta*, 2020, **271**, 96–115.
13 T. E. Flores-Guia, L. F. Cano Salazar, A. Martínez-Luévanos and J. Claudio-Rizo, *Handbook of Nanomaterials and Nanocomposites for Energy and Environmental Applications*, 2021, pp. 2409–2428.
14 H. Yin, B. Lanson, S. Zhang, L. Liu, C. L. Peacock, J. E. Post, M. Zhu, W. Li, Q. Wang and J. Zhang, *Geochim. Cosmochim. Acta*, 2022, **333**, 200–215.
15 A. G. Newton and K. D. Kwon, *Geochim. Cosmochim. Acta*, 2020, **291**, 92–109.
16 F. Li, H. Yin, T. Zhu and W. Zhuang, *Eco-Environ. & Health*, 2024, **3**, 89–106.
17 P. R. Garces Goncalves Jr, H. A. De Abreu and H. l. A. Duarte, *J. Phys. Chem. C*, 2018, **122**, 20841–20849.
18 M. C. Kemei, J. K. Harada, R. Seshadri and M. R. Suchomel, *Phys. Rev. B:Condens. Matter Mater. Phys.*, 2014, **90**, 064418.
19 S. V. Ovsyannikov, A. A. Aslandukova, A. Aslandukov, S. Chariton, A. A. Tsirlin, I. V. Korobeynikov, N. V. Morozova, T. Fedotenko, S. Khandarkhaeva and L. Dubrovinsky, *Inorg. Chem.*, 2021, **60**, 13440–13452.
20 T. Kohler, T. Armbruster and E. Libowitzky, *J. Solid State Chem.*, 1997, **133**, 486–500.
21 Y. O. Yesilbag, F. N. Tuzluca and M. Ertugrul, *J. Mater. Sci.: Mater. Electron.*, 2019, **30**, 8201–8209.
22 L. G. Teoh and K.-D. Li, *Mater. Trans.*, 2012, **53**, 2135–2140.
23 R. Dubey, Y. Rajesh and M. More, *Mater. Today: Proc.*, 2015, **2**, 3575–3579.
24 J. Kurian and M. J. Mathew, *J. Magn. Magn. Mater.*, 2018, **451**, 121–130.
25 H. Lee, M. Y. Song, J. Jurng and Y.-K. Park, *Powder Technol.*, 2011, **214**, 64–68.
26 H. Naser, M. Alghoul, M. K. Hossain, N. Asim, M. Abdullah, M. S. Ali, F. G. Alzubi and N. Amin, *J. Nanopart. Res.*, 2019, **21**, 1–28.

27 M. Pišlová, M. Kalbacova, L. Vrabcová, P. Slepička, Z. Kolská and V. Švorčík, *Dig. J. Nanomater. Bios.*, 2018, **13**, 1035–1044.
28 M. Gautam, J. O. Kim and C. S. Yong, *J. Pharm. Invest.*, 2021, **51**, 361–375.
29 X. Fang, J. Li, B. Ren, Y. Huang, D. Wang, Z. Liao, Q. Li, L. Wang and D. D. Dionysiou, *J. Membr. Sci.*, 2019, **579**, 190–198.
30 D. B. Raudabaugh, *et al., Nanomater. Nanotechnol.*, 2013, **3**, 2.
31 M. Shu, F. He, Z. Li, X. Zhu, Y. Ma, Z. Zhou, Z. Yang, F. Gao and M. Zeng, *Nanoscale Res. Lett.*, 2020, **15**, 1–9.
32 T. Aswani, S. Reshmi and T. Suchithra, *Microbial Nanobionics: Volume 1, State-Of-The-Art*, 2019, pp. 127–140.
33 S. Azizi, M. Mahdavi Shahri and R. Mohamad, *Molecules*, 2017, **22**, 831.
34 S. Ekrikaya, E. Yilmaz, C. Celik, S. Demirbuga, N. Ildiz, A. Demirbas and I. Ocsoy, *J. Biotechnol.*, 2021, **341**, 155–162.
35 R. Verma, A. Chauhan, S. Kumari, R. Jasrotia, A. Ali, C. Gopalakrishnan, R. Kumar and S. Ghotekar, *Chem. Pap.*, 2023, 1–11.
36 A. Chauhan, R. Verma, S. Kumari, A. Sharma, P. Shandilya, X. Li, K. M. Batoo, A. Imran, S. Kulshrestha and R. Kumar, *Sci. Rep.*, 2020, **10**, 7881.
37 V. Mohammadzadeh, M. Barani, M. S. Amiri, M. E. T. Yazdi, M. Hassanisaadi, A. Rahdar and R. S. Varma, *Sustainable Chem. Pharm.*, 2022, **25**, 100606.
38 I. Ijaz, E. Gilani, A. Nazir and A. Bukhari, *Green Chem. Lett. Rev.*, 2020, **13**, 223–245.
39 Y. Liu, W. Zhang, C. Xu and X. Li, *Int. J. Mol. Sci.*, 2016, **17**, 1983.
40 R. A. Syahputra, H. Helen, M. C. Gunawan, Z. D. Utari, A. Dalimunthe, E. Salim, M. Bastian, N. A. Taslim, P. Pitriani and S. E. Nugraha, *J. Agric. Food Res.*, 2025, **22**, 102091.
41 T. Khouya, M. Ramchoun, H. Elbouny, A. Hmidani and C. Alem, *J. Ethnopharmacol.*, 2022, **296**, 115473.
42 Y.-G. Hwang, J.-J. Lee, A.-R. Kim and M.-Y. Lee, *J. Life Sci.*, 2010, **20**, 1625–1633.
43 D. A. Infante-Rodríguez, M. J. Aguilar-Méndez, C. Landa-Cansigno, S. G. Vásquez-Morales, A. C. Velázquez-Narváez, J. E. Valenzuela-González, A. L. Kiel-Martínez, J. L. Monribot-Villanueva and J. A. Guerrero-Analco, *Bot. Sci.*, 2024, **102**, 1231–1250.
44 S. Taniguchi, Y. Imayoshi, E. Kobayashi, Y. Takamatsu, H. Ito, T. Hatano, H. Sakagami, H. Tokuda, H. Nishino and D. Sugita, *Phytochemistry*, 2002, **59**, 315–323.
45 X. Zhu, L. Wang, T. Zhao and Q. Jiang, *J. Ethnopharmacol.*, 2022, **298**, 115566.
46 H. Lv, J. Chen, W.-L. Li and H.-Q. Zhang, *Zhongyaocai*, 2008, **31**, 1351–1354.
47 B. Chen, P. Long, Y. Sun, Q. Meng, X. Liu, H. Cui, Q. Lv and L. Zhang, *Food Funct.*, 2017, **8**, 687–694.
48 A. A. Barzinjy, S. M. Hamad, A. F. Abdulrahman, S. J. Biro and A. A. Ghafor, *Curr. Org. Synth.*, 2020, **17**(7), 558–566, DOI: 10.2174/1570179417666200628140547.
49 H. G. Gebretnsae and Y. T. Gebreslassie, *Nanoscale Res. Lett.*, 2021, **16**(1), 97, DOI: 10.1186/s11671-021-03555-6.
50 S. A. Miraeez and R. Y. Mohammed, *Int. J. Environ. Anal. Chem.*, 2026, **106**, 378–409.
51 A. J. Enitan, L. I. Oduola and O. T. Olorunyomi, *Lek. Sirovine*, 2021, **41**, 17–21.
52 A. Al Ghasham, M. Al Muzaini, K. A. Qureshi, G. O. Elhassan, R. A. Khan, S. A. Farhana, S. Hashmi, E. El-Agamy and W. E. Abdallah, *Int. J. Pharm. Res. Allied Sci.*, 2017, **6**(3), 33–46.
53 K. S. Banu and L. Cathrine, *Int. j. adv. res. chem. sci.*, 2015, **2**, 25–32.
54 R. Verma, S. Singh, B. Priya, S. Jha and L. Rani, *Res. J. Agric. Sci.*, 2023, **14**, 1541–1546.
55 R. J. Ruch, S.-j. Cheng and J. E. Klaunig, *Carcinogenesis*, 1989, **10**, 1003–1008.
56 V. Chooranam, *Asian J. Pharm. Clin. Res.*, 2017, **10**, 111–116.
57 J. R. Shaikh and M. Patil, *Int. J. Chem. Stud.*, 2020, **8**, 603–608.
58 S. Deshpande, *J. Pharmacogn. Phytochem.*, 2013, **1**, 23–27.
59 N. Raaman, *Phytochemical Techniques*, New India Publishing, 2006.
60 A. H. Al-Mossawi and Z. S. Al-Garawi, *Qualitative tests of amino acids and proteins and enzyme kinetics*, Mustansiriyah University, Baghdad, 2018.
61 A. R. Gollakota, V. S. Munagapati, V. Volli, S. Gautam, J.-C. Wen and C.-M. Shu, *J. Hazard. Mater.*, 2021, **416**, 125925.
62 Y. Wang, L. He, Y. Li, L. Jing, J. Wang and X. Li, *J. Alloys Compd.*, 2020, **828**, 154340.
63 Z. Ishak and D. Kumar, *Tropical Aquatic and Soil Pollution*, 2022, **2**, 1–12.
64 T. R. Das and P. K. Sharma, *Mater. Sci. Semicond. Process.*, 2020, **105**, 104721.
65 Y. He, D. B. Jiang, J. Chen and Y. X. Zhang, *J. Colloid Interface Sci.*, 2018, **510**, 207–220.
66 M. A. Al-Ghouti and M. M. Razavi, *Environ. Technol. Innovation*, 2020, **17**, 100614.
67 F. Ahmadijokani, R. Mohammadkhani, S. Ahmadipouya, A. Shokrgozar, M. Rezakazemi, H. Molavi, T. M. Aminabhavi and M. Arjmand, *Chem. Eng. J.*, 2020, **399**, 125346.
68 M. Kasbaji, M. Mennani, N. Grimi, F. J. Barba, M. Oubenali, M. J. Simirgiotis, M. Mbarki and A. Moubarik, *Process Biochem.*, 2022, **120**, 213–226.
69 K. Naseri and A. Allahverdi, *Res. Chem. Intermed.*, 2019, **45**, 4863–4883.
70 D. Balarak, F. Kord Mostafapour, H. Azarpira and A. Joghataei, *Past Name: British Journal of Pharmaceutical Research*, Past ISSN: 2231-2919, 2017, pp. 1–9.
71 H. N. Tran, S.-J. You and H.-P. Chao, *J. Environ. Chem. Eng.*, 2016, **4**, 2671–2682.
72 M. Alizadeh, S. J. Peighambardoust, R. Foroutan, H. Azimi and B. Ramavandi, *Environ. Res.*, 2022, **212**, 113242.
73 R. Foroutan, S. J. Peighambardoust, R. Mohammadi, S. H. Peighambardoust and B. Ramavandi, *Environ. Res.*, 2022, **211**, 113020.
74 G. Yin, X. Song, L. Tao, B. Sarkar, A. K. Sarmah, W. Zhang, Q. Lin, R. Xiao, Q. Liu and H. Wang, *Chem. Eng. J.*, 2020, **389**, 124465.

75 S. I. Al-Saeedi, A. Areej, M. T. Qamar, A. Alhujaily, S. Iqbal, M. T. Alotaibi, M. Aslam, M. A. Qayyum, A. Bahadur and N. S. Awwad, *Front. environ. sci.*, 2023, **11**, 1156475.
76 T. Chouchane, O. Khireddine and A. Boukari, *J. Eng. Appl. Sci.*, 2021, **68**, 34.
77 M. I. Khan, S. Sufian, F. Hassan, R. Shamsuddin and M. Farooq, *RSC Adv.*, 2025, **15**, 1989–2010.
78 S. Salvestrini, L. Ambrosone and F.-D. Kopinke, *J. Mol. Liq.*, 2022, **352**, 118762.
79 H. Deng, Y. Wu, L. Li, P. Wang, K. Fang, J. Li, D. Hao, H. Zhu, Q. Wang and Q. Li, *Sep. Purif. Technol.*, 2025, **354**, 129455.
80 P. Patil, G. Jeppu, M. S. Vallabha and C. R. Girish, *Environ. Sci. Pollut. Res.*, 2024, **31**, 67442–67460.
81 N. M. Hosny and A. Dahshan, *Mater. Chem. Phys.*, 2012, **137**, 637–643.
82 M. Ahmad, M. Ahmad, M. H. Aziz and M. Asif, *Heliyon*, 2024, **10**(5), 1–15, DOI: 10.1016/j.heliyon.2024.e26708.
83 S. Ayyappan, G. Panneerselvam, M. Antony and J. Philip, *Mater. Chem. Phys.*, 2011, **130**, 1300–1306.
84 K. V. Chandekar and K. Kant, *Phys. B*, 2018, **545**, 536–548.
85 Z. Xu, W. Zhao, J. Liu and J. Fan, *Magnetochemistry*, 2023, **9**, 146.
86 A. Sharma, N. Dhiman, B. P. Singh and A. K. Gathania, *Mater. Res. Express*, 2014, **1**, 025042.
87 W. Yang, Q. Wang, K. Xu, Y. Yin, H. Bao, X. Li, L. Niu and S. Chen, *Materials*, 2017, **10**, 956.
88 Z. Sanaei, T. Shahrabi and B. Ramezanzadeh, *Dyes Pigm.*, 2017, **139**, 218–232.
89 S. Nikpour, M. Ramezanzadeh, G. Bahlakeh, B. Ramezanzadeh and M. Mahdavian, *Constr. Build. Mater.*, 2019, **220**, 161–176.
90 Q. Abbas, *J. Nanomater. Mol. Nanotechnol.*, 2019, **8**, 1–3.
91 S. Ma, L. Zheng, Y. Shi, L. Jia and X. Xu, *J. Mater. Sci.: Mater. Electron.*, 2018, **29**, 16921–16931.
92 T. Sarkar, S. Kundu, G. Ghorai, P. K. Sahoo and A. Bhattacharjee, *Adv. Nat. Sci.:Nanosci. Nanotechnol.*, 2023, **14**, 035001.
93 Y. Kong, R. Jiao, S. Zeng, C. Cui, H. Li, S. Xu and L. Wang, *Nanomaterials*, 2020, **10**, 367.
94 M. K. Goswami and A. Srivastava, *J. Appl. Polym. Sci.*, 2025, **142**, e56713.
95 C. B. Godiya, Y. Xiao and X. Lu, *Int. J. Biol. Macromol.*, 2020, **144**, 671–681.
96 E. M. Saad, M. Wagdy and A. S. Orabi, *Sci. Rep.*, 2024, **14**, 23614.
97 C. Aniagor, A. Hashem, N. Badawy and A. Aly, *Hybrid Adv.*, 2023, **3**, DOI: 10.1016/j.hybadv.2023.100047.
98 F. A. Adam, M. Ghoniem, M. Diawara, S. Rahali, B. Y. Abdulkhair, M. Elamin, M. A. B. Aissa and M. Seydou, *RSC Adv.*, 2022, **12**, 24786–24803.
99 T. Chouchane, M. T. Abedghars, S. Chouchane and A. Boukari, *Kuwait J. Sci.*, 2024, **51**, 100210.
100 C. Toufik, K. Ouahida, C. Sana and B. Aatmane, *Anal. Bioanal. Chem. Res.*, 2023, **10**, 251–268.
101 C. Li, X. Li, Y. Yu, Q. Zhang, L. Li, H. Zhong and S. Wang, *J. Ind. Eng. Chem.*, 2022, **105**, 63–73.
102 T. C. Egbosiuba, T. Q. Tran, K. Arole, Y. Zhang, C. E. Enyoh, S. Mustapha, J. O. Tijani, V. K. Yadav, V. C. Anadebe and A. S. Abdulkareem, *Results Eng.*, 2024, **22**, 102073.
103 O. Bayram, U. Özkan, S. Kardeş, E. Moral, F. Göde and E. Pehlivan, *Chem. Ecol.*, 2025, **41**, 528–551.
104 D. Awang Chee, N. Kamaludin, M. Soffian, F. Abdul Halim and M. Mohamed Amin, *Int. J. Environ. Sci. Technol.*, 2025, **22**, 1591–1608.
105 S. K. D. Al Shariar Hasan, A. Bashar, P. K. Dhar and R. Haque, *Extraction*, 2025, **9**, 10.
106 O. Bayram, U. Özkan, İ. Pekgözlü and F. Göde, *Sep. Sci. Technol.*, 2025, **60**, 1406–1420.
107 Y. Zhang, W. Zhang, G. Yang, Z. Chen and W. Zhang, *Microporous Mesoporous Mater.*, 2025, **392**, 113623.
108 S. Dutta, M. Jahan, N. Kaur, S. Barna, N. Sathi, R. Sultana, P. Dhar, M. Al Mamun, S. Chakrabarty and M. Amin, *Int. J. Environ. Sci. Technol.*, 2025, **22**, 1865–1890.
109 A. S. Abdulhameed, S. Abdullah, A. A. Al-Masud, M. Abualhaija and S. Algburi, *Polym. Bull.*, 2025, 1–28.
110 S. D. Barna, M. N. Jahan, S. R. Sium, A. Nag, M. H. Ali and S. K. Dutta, *Discov. chem.*, 2024, **1**, 38.
111 O. Bayram, U. Özkan, F. Göde, S. Coşkun and H. T. Şahin, *J. Dispersion Sci. Technol.*, 2025, **46**, 1737–1746.
112 T. S. Alomar, N. AlMasoud, G. Sharma, Z. A. Alothman and M. Naushad, *J. Mol. Liq.*, 2021, **336**, 116274.
113 Y. He, D. B. Jiang, J. Chen, D. Y. Jiang and Y. X. Zhang, *J. Colloid Interface Sci.*, 2018, **510**, 207–220.
114 T. Chouchane, O. Khireddine, S. Chouchane, M. T. Abedghars and H. Meradi, *Turk. J. Chem.*, 2024, **48**, 867–884.
115 F. Barracco, E. Parisi, G. Pipitone, E. Simone, S. Bensaid and D. Fino, *Int. J. Environ. Sci. Technol.*, 2024, **21**, 6513–6530.
116 K. Ezeh, I. Ogbu, K. Akpomie, N. Ojukwu and J. Ibe, *Pac. J. Sci. Technol.*, 2017, **18**, 251–264.
117 A. Hashem, C. O. Aniagor, S. Farag, M. Fikry, A. Aly and A. Amr, *Waste Management Bulletin*, 2024, **2**, 172–183.
118 S. K. M. Rozi, K. Y. Qin, H. N. A. Halim, M. M. H. Al-Rajabi and A. R. Ishak, *Biomass Convers. Biorefin.*, 2025, 1–19.
119 C. R. Girish, *Chem. Pap.*, 2025, **79**, 5687–5706.
120 P. Saha and S. Chowdhury, *Thermodynamics*, 2011, **16**, 349–364.
121 A. S. Abdulhameed, S. Abdullah, A. A. Al-Masud, M. Abualhaija and S. Algburi, *Polym. Bull.*, 2025, **82**, 6763–6790.
122 K. Polley and J. Bera, *Int. J. Environ. Anal. Chem.*, 2024, **104**, 5620–5637.
123 S. Mariska, J.-L. Lin, T. T. A. Tuyet, N. D. Hai and H.-P. Chao, *Appl. Water Sci.*, 2024, **14**, 95.
124 P. Arabkhani, N. Sadegh and A. Asfaram, *Microchem. J.*, 2023, **184**, 108149.